[American Journal of Science, Vol. 306, February, 2006, P. 103–134]

CONTROLS ON HEAT FLOW, FLUID MIGRATION, AND MASSIVE SULFIDE FORMATION OF AN OFF-AXIS HYDROTHERMAL SYSTEM—THE LAU BASIN PERSPECTIVE

CHRISTIAN SCHARDT*†, ROSS LARGE*, and JIANWEN YANG**

ABSTRACT. A numerical model has been developed to investigate heat and fluid migration in a modern off-axis seafloor hydrothermal system, that is, hydrothermal activity and fluid discharge distal to an axial magma chamber emphasizing model geometry, rock/fault properties and fault distribution. The model is based on geophysical data and seafloor observations of the Lau back-arc basin and results suggest a different hydrothermal convection scheme than axial hydrothermal systems. Major hydrothermal activity is predicted to occur at topographic highs due to significant fluid migration along inferred basement topography off-axis with associated permeability differences. Major hydrothermal fluid discharge occurs at off-axis topographic elevated positions with temperatures (150°C - 450°C) and exit fluid velocities (~4 m/s), in good agreement with seafloor observation and theoretical calculations. Heuristic mass calculations pertaining to the formation of massive sulfide deposits imply that a significant base metal sulfide deposit (5 Mt at 10% Cu + Zn) may form in less than 6,000 years, assuming a fluid containing a maximum of 10 ppm base metals and a deposition efficiency of 10 percent. The size and distribution patterns of massive sulfide deposits are determined primarily by fault distribution, provided that adequate fluid flow pathways and heat supply exist.

INTRODUCTION

A significant amount of work has been devoted to the study of seafloor hydrothermal systems and the formation of massive sulfide ore bodies using computer modeling. This includes hydrothermal convection in the oceanic crust (for example, Parmentier and Spooner, 1978; Lowell, 1980; Strens and Cann, 1986; Davis and others, 1996; Rabinowicz and others, 1998; Yang, 2002; Schardt and others, 2005), at mid-ocean ridge spreading centers (for example, Fehn and Cathles, 1979; Lowell and Burnell, 1991; Cathles, 1993; Fisher and others, 1997; Fontaine and others, 2001; Fisher, 2004) as well as experimental work (for example, Solomon and others, 1987; Martin and Lowell, 1997).

Numerical modeling is a useful tool to quantify physical and chemical processes that occur in hydrothermal systems, which are inaccessible, too complex, or too slow to observe. Together, with field data and laboratory measurements, modeling results can be used to better understand the evolution of hydrothermal systems and the genesis of associated massive sulfide deposits. Computer modeling has been used successfully to investigate a number of important aspects related to submarine heat and fluid flow such as rock permeability, the role of basement relief or the importance of fault structures (for example, Strens and Cann, 1982; Rosenberg and Spera, 1992; Fisher and Becker, 1995; Snelgrove and Forster, 1996; Yang, 2002; Schardt and others, 2005). However, most of these studies investigated heat and fluid flow under idealized conditions and few studies integrate all of these features. Recent discoveries and ongoing research in this field permit computer simulations of heat and fluid transport under more realistic conditions, that is the inclusion of detailed topography or the reconstruction of tectonic framework at the time of formation.

*CODES ARC Centre of Excellence in Ore Deposits, University of Tasmania, Private Bag 79, Hobart, Tasmania, Australia 7001.

**Department of Earth Sciences, University of Windsor, Windsor, Ontario, N9B 3P4, Canada

†Present address: Department of Earth and Planetary Sciences, The John Hopkins University, Baltimore, Maryland, 21218, USA; cschard1@jhu.edu

In this study we develop a numerical model that combines features such as surface/basement topography, fault structure/distribution, and rock/fault permeability to investigate their influence on heat and fluid migration in the ocean's crust and its consequences for hydrothermal fluid discharge and the formation of volcanic-hosted massive sulfide (VHMS) deposits. In particular, this model investigates heat and fluid flow in off-axis regions, defined as distinct areas away from rift structures or magma chambers, as potential sites for ore body formation. A sensitivity analysis tests a variety of geological and structural features and their influence on the magnitude and direction of heat and fluid flow. Findings from this study will help to better define the location and likely size of massive sulfide mineralization on the seafloor and aid future exploration efforts in modern and ancient volcanic terrains. The Lau Basin has been selected for this study because it has been well studied (Collier and Sinha, 1992; Fouquet and others, 1993; Parson and others, 1994; Kamenetsky and others, 1997; Herzig and others, 1998; Turner and others, 1999), and results provide vital information used to constrain the numerical model used here such as the structure, topography, geology, and tectonics of the basin.

GEOLOGIC SETTING

The Lau Basin is a typical example of an active back-arc basin formed by arc splitting, separating the active Tofua volcanic arc in the east from the remnant arc (the Lau Ridge) in the west (Fouquet and others, 1993; Wiedicke and Collier, 1993; Tappin and others, 1994; fig. 1). It is a triangular-shaped shallow basin (2 to 3 km), about 100 km to 200 km wide, and about 400 km long with an irregular horst and graben topography (Parson and others, 1994; Hodkinson and Cronan, 1998). In addition, three major active spreading ridges are found in the central Lau Basin: the Central Lau Spreading Center (CLSC) to the north, the Eastern Lau Spreading Center (ELSC) and the Valu Fa Ridge to the south (Macpherson and Mattey, 1998; Kent and others, 2002). While sediment thickness ranges from a thin blanket (~100 m) to about 700 m in regions close to either bordering ridge (Gill, 1976), the floor of the Lau basin consists of tholeiitic and fractionated basalts generated through back-arc spreading and rifted island-arc basaltic andesitic to dacitic crust of Oligocene to Pliocene age (Parson and others, 1994; Rothwell, 1998). Rock samples from the adjacent Valu Fa ridge are mainly andesitic basalts, andesites, and rhyodacites with distinct geochemical signatures of both back-arc basin and active island arc (Sunkel, 1990; Frenzel and others, 1990; Vallier and others, 1991). The morphotectonic features are similar to that of fast-spreading ridges, with mostly inward facing fault scarps with throws <300 m, trending as continuous lineaments up to 40 km subparallel to the ridge axis (Parson and Wright, 1996). The Lau Basin is presently opening at about 124 to 144 mm/yr (Hawkins, 1995) and a number of active hydrothermal areas and polymetallic deposits from the Lau Basin have been described by Herzig and others (1990), Fouquet and others (1993), and Herzig and others (1993). Earlier studies provide good geophysical and topographical information (Riech and others, 1990; Tappin and others, 1994; Turner and others, 1999) and together with data from Morton and Sleep (1985), Collier and Sinha (1992), Fouquet and others (1993), Tappin and others (1994), Parson and Wright (1996), and Turner and others (1999) a schematic 2-D cross-sectional model section was constructed that includes a simplified stratigraphy and a simplified topography based on seismic profiles of Parson and others (1994), resembling geological conditions in the active, rifting part of the Lau Basin such as the Valu Fa ridge.

Model Geometry and Structure

Figure 2 shows the geometry and stratigraphy of the model section: a 7 by 60 km solution domain consisting of 58 columns and 28 rows with a total of 1,276 rectangular

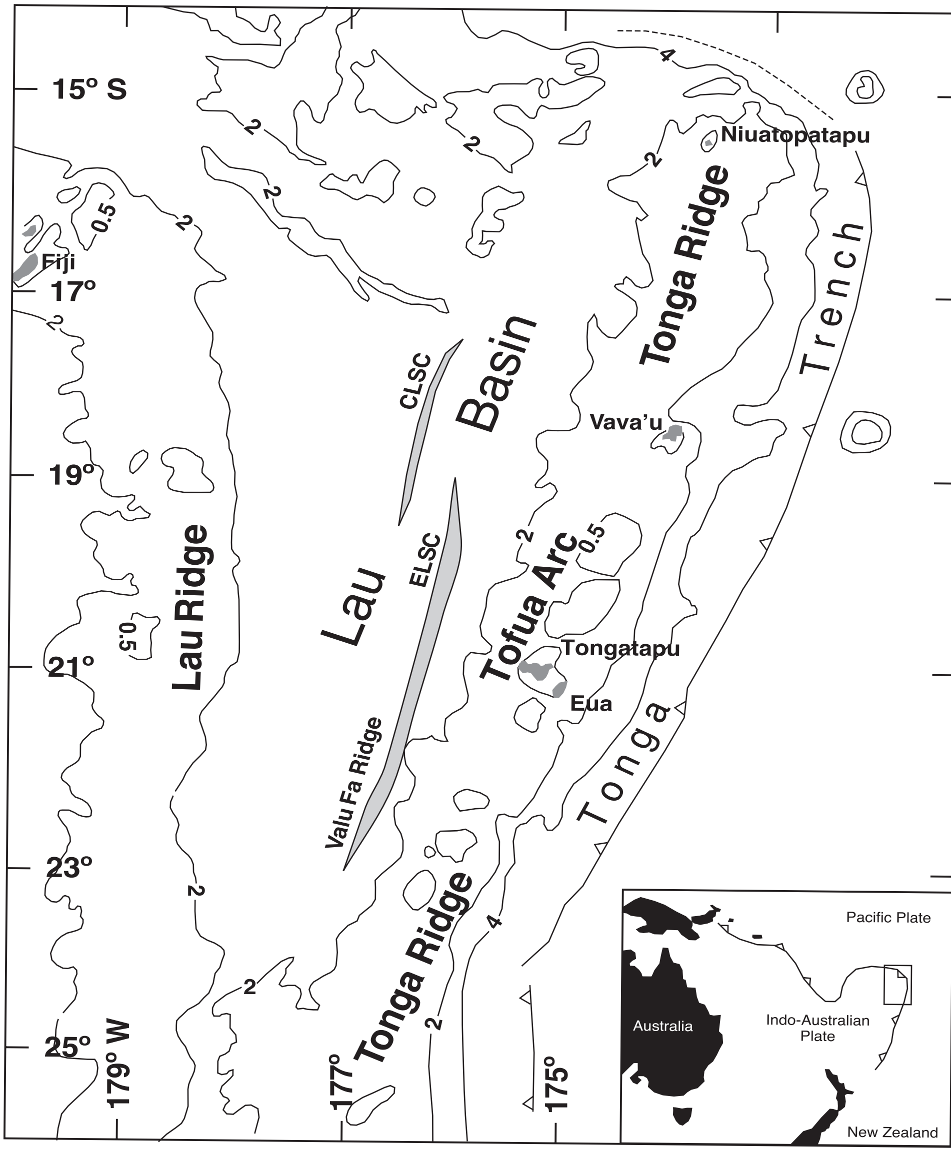

Fig. 1. Location of the Lau Basin and main topographic features (adapted from Tappin and others, 1994; MacPherson and Mattey, 1998). Contours show water depth in kilometers.

elements. The model has a distinct graben topography and typical seafloor stratigraphy and is symmetrical in terms of fault distribution, depth, and hydrostratigraphy. A 200 m thin sediment package covering a 300 m thick breccia sequence overlies an 800 m thick andesite layer based on data from Fouquet and others (1993), Parson and others (1994), and Lagabrielle and others (1994). The underlying sheeted dikes range from 1.4 to 1.9 km in thickness and the basement consists of layered gabbros and a magma chamber 2.4 km below the seafloor, as described by Collier and Sinha (1992). A number of inward-facing faults, extending from the surface of the model into the sheeted dike zone (Parson and others, 1994; Parson and Wright, 1996), are incorpo-

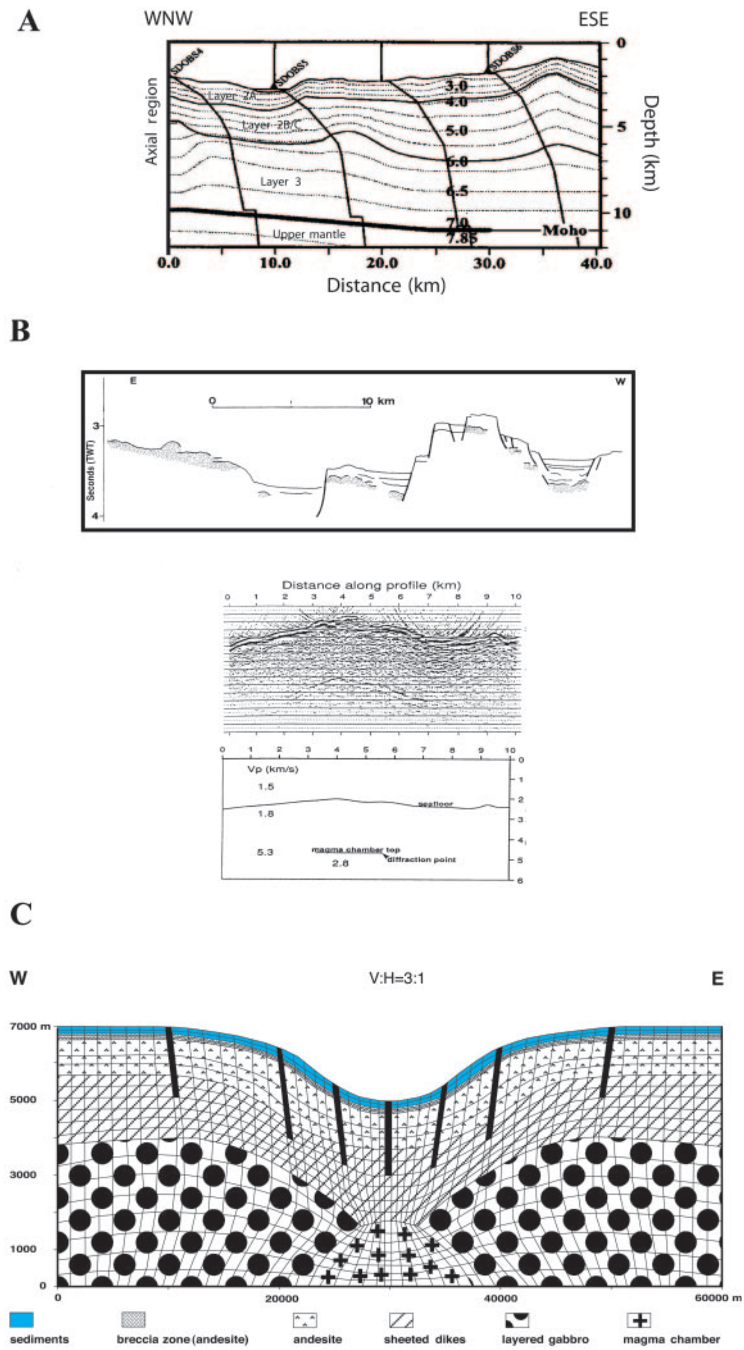

Fig. 2. (A) Best-fitting velocity-depth model from seismic results for part of the Lau Basin. Dotted lines are isovelocity contours (km/s) and solid lines show topography, inferred sediments, layer boundaries, and the seismic Moho; vertical lines show digital ocean-bottom seismometers (SDOB) used (simplified from Turner and others, 1999). (B) Seismic data from the Lau Basin from Collier and Sinha (1992) illustrating fault spacing, extent, and depth of magma chamber representing the axial region. (C) Numerical solution domain of the Lau Basin model showing stratigraphy, geometry, and structure. To illustrate heat and fluid flow, as well as the distribution of water-rock ratios, a vertical exaggeration (V:H) of 3:1 is used. The numerical solution domain was constructed to represent a simplified model of part of the Lau Basin containing a central magma chamber and lateral regions with elevated topography and fault structures based on the data shown here as well as additional information from Fouquet and others (1991).

TABLE 1

Initial rock properties of the Lau Basin model

Rock unit	Permeability (m^2)	Porosity (%)	Thermal conductivity (W/m*C)	Source
Sediments	$5x10^{-18}$	50	1.5	Becker and others (1985) Fisher and Narasimhan (1991) Snelgrove and Forster (1996)
Breccia zone	$2.5x10^{-16}$	12	1.5	estimated
Andesite	$2.5x10^{-17}$	8	1.5	Becker (1990) Bruns and Lavoie (1994) Fisher and others (1997) Christensen and Itturino (2004)
Sheeted dikes	$1.6x10^{-17}$	2	2.0	Becker and others (1985) Becker and others (1989) Salisbury and others (1985)
Gabbro	$9.6x10^{-19}$	1	2.0	Becker and others (1989) Goldberg and others (1991)
Faults	$2.5x10^{-14}$	30	2.0	estimated

Note: Anisotropic rock permeability has been applied to the breccia zone and andesite layer; values listed here are permeability values in the vertical direction, while permeability in the horizontal direction are two order of magnitude higher.

rated into the numerical mesh as regions of higher permeability to facilitate fluid flow and fluid discharge. Fault width has been set to 400 m (Schardt, ms, 2004) and faults are spaced 5 and 10 km apart respectively, based on seismic data from the Lau Basin obtained by Parson and others (1994).

Initial and Boundary Conditions

Rock properties and initial conditions at the start of the simulations are shown in table 1. Average to minimum values chosen from the literature assume unfractured volcanic and magmatic rocks with low to average permeability. This choice allows the system to be tested under 'conservative' conditions and provides a reference point for a sensitivity analysis. Since sediments at depth are considered impermeable with respect to fluid flow (Fisher and others, 1994; Davis and others, 1996; Giambalvo and others, 2000) it is assumed that the sediment cover in general acts as a low permeability barrier and thus low permeability values are applied. This is also evident in field observations, that is most fluid discharge occurs along fault structures and only secondary by migration through sediment packages (Brauhart and others, 1998; Elderfield and others, 2004). To allow significant lateral fluid flow and associated heat transport, anisotropic rock permeability for the breccia zone and the andesitic layer was assumed, where horizontal permeability is larger than vertical permeability with $K_{horizontal} = 100 * K_{vertical}$ based on preliminary calculations and previous work (Rosenberg and others, 1993; Dickson and others, 1995; Fisher and Becker, 1995; Fisher, 1998; Schardt and others, 2005). All other rock units possess isotropic permeability values, since they either don't exhibit significant fluid flow (gabbros) or flow patterns remain unaffected (sheeted dikes) by permeability differences investigated here (one order of magnitude). Although it is reasonable to assume that sheeted dikes may exhibit vertical permeability anisotropy, this has not been tested here, because it is unlikely to greatly influence fluid flow patterns or the general discharge behavior of individual faults.

For a 2-D model there are 4 boundaries, which must be defined in terms of heat and fluid flow exchange. Since this model simulates the convection of hydrothermal fluids near the seafloor, covered with low-permeability sediments, the top boundary is assigned a constant temperature of 0°C and a free-flow boundary, that is fluids are allowed to enter and leave across the whole top boundary. In addition, a constant hydraulic head (3,000 m) is applied at the top boundary based on average water depth for the basin (Hodkinson and Cronan, 1998). Side boundaries are closed to heat and fluid flux, as is the lower boundary. While mafic and ultramafic intrusions such as seafloor magma chambers can reach temperatures of ~1,250°C (Fehn and Cathles, 1979; Sparks, 1986; Barrie and others, 1999b) an average heater temperature of 1,200°C is used here for the magma chamber to simulate mantle-derived melts underlying a thin seafloor crust; other sections of the lower boundary, represented by layered gabbro, are set to 800°C (see fig. 2). Both the magma chamber and lower boundary are allowed to cool from the beginning of the calculations. Instead of a conductive boundary layer to control heat transfer at depth, the rate of cooling depends on the magnitude of hydrothermal circulation and subsequent cooling by circulating seawater via heat conduction and convection specified in the computer code (see Yang and others, 1998; Yang and Large, 2001).

The initial temperature distribution within the solution domain is linear, from 0°C at the top of the model section to 1,200°C and 800°C respectively. Initial fluid velocity is assumed to be zero throughout the system and density and viscosity of circulating fluids are controlled by temperature.

Numerical Modeling

Numerical computation of hydrothermal fluid flow involves the solution of continuum-based coupled time-dependent mass (fluid) and energy (heat) conservation differential equations, which in turn are influenced by temperature and pressure on boundaries (for example, Fehn and Cathles, 1979; Fisher and others, 1990; Lowell and others, 1995; after Yang and others, 1998). Detailed derivation of these governing equations is not provided here, but can be found elsewhere (for example, Bear, 1972; Raffensperger and Garven, 1995). The finite element technique in conjunction with the Galerkin's method is widely used in groundwater modeling (for example, Huyakorn and Pinder, 1986) and hydrothermal fluid circulation (for example, Yang and others, 2001) and will be applied here. Faults are incorporated into the numerical grid as regions of elevated permeability to facilitate fluid flow within fault regions (see fig. 2). Computer software as described by Yang and others (1998) and Yang and Large (2001) is used here to simulate heat and fluid transport in the Lau Basin model. No supercritical and/or multiphase flow is considered here and fluids are defined by properties of pure water due to software restrictions. In this study, time-stepping is organized in time-periods, that is within each time-period the timestep is constant and the Crank-Nicolson method is used to facilitate time-stepping. Time-periods range from 100 to 100,000 years while time steps vary from 10 years to 1,000 years; both increase with simulation progress. Numerical instabilities occur only for very high fault and/or rock permeabilities ($>10^{-13}$ m^2) due to software restrictions; results from these conditions have therefore not been included.

Following simulations with averaged rock properties (see table 1), a sensitivity analysis was performed by varying key rock properties (permeability, porosity, thermal conductivity; see table 2) based on published data and fault permeability limited by software restrictions to investigate the sensitivity and response of the hydrothermal system to changing hydraulic conditions. Theoretical constraints applied here include the assumption of local equilibrium and, apart from the heterogeneous permeability distribution discussed earlier, a uniform thermal conductivity and porosity distribution for each individual rock unit has been assumed. Results presented here comprise a

Table 2

Range of physical rock property values used for the sensitivity analysis

Rock unit	Permeability variation (m^2)	Porosity variation (%)	Thermal conductivity variation (W/m*C)
Sediments	$5x10^{-18}$	50	1.5
Breccia zone	$2.5x10^{-15}$ - $2.5x10^{-17}$	1 - 20	1.2 - 3.7
Andesite	$2.5x10^{-16}$ - $2.5x10^{-18}$	1 - 20	1.2 - 3.2
Sheeted dikes	$1x10^{-17}$	2	2.0
Gabbro	$1x10^{-18}$	1	2.0
Faults	$1x10^{-12}$ - $1x10^{-16}$	30	2.0

Note: No permeability changes have been made to sheeted dikes and gabbro due to their assumed 'impermeable' nature.

selection of more than thirty different models to demonstrate the most important findings.

results

Heat distribution, fluid velocity, and water-rock ratios for initial conditions after 10,000 years are shown in figure 3. Fluid discharge is predicted to occur mainly through outer faults with discharge temperatures of ~350°C and recharge via the inner faults in the topographic depression (fig. 3A). Main fluid flow occurs via fault structures as well as within the breccia zone and the sheeted dike-gabbro interface (fig. 3B). The middle fault (fault 4) shows fluid discharge at lower rock permeabilities and is predicted to turn into a recharge zone at high rock permeability (see table 3). While all simulations predict short fluid recharge through fault 4 at the beginning of simulations, high rock permeabilities appear to enable sustained fluid recharge for fault 4. This may be comparable to conditions at the onset of the hydrothermal system, where fault permeabilities increase due to the expansion of the heat source at depth (Schardt, ms, 2004).

Faults 2 to 6 only exhibit short periods of fluid discharge in the early stages of the simulations; they are mainly recharge zones. The convection system is controlled by buoyancy-driven fluid flow in the central part and basement highs away from the center of the section, predicting major fluid flow up the outer faults and the central fault 4, and fluid recharge through inner faults. To characterize alteration as a function of fluid flow, mass water-rock ratios, defined as the amount of fluid passing through a control volume of rock, have been calculated on a cumulative basis, reflecting the degree of alteration over time and by analogy the preferred fluid flow pathways. The general extent of alteration can then be evaluated by assigning highest water-rock ratios to zones of most intense alteration. This is only a first approximation of alteration intensity, as other factors such as pH, temperature, and chemistry of the fluid will also influence the intensity of mineralogical alteration. Figure 3C shows that most intense alteration, reflected by high water-rock ratios (100-600) occurs around faults, while the overall water-rock ratios elsewhere are much lower, about 0.5 to 4.

sensitivity analysis

The sensitivity analysis was designed to investigate the influence of rock properties (permeability, thermal conductivity, porosity) and fault properties (permeability, distribution) on heat and fluid flow, fluid velocity, discharge temperatures, and alteration zonation (see table 2).

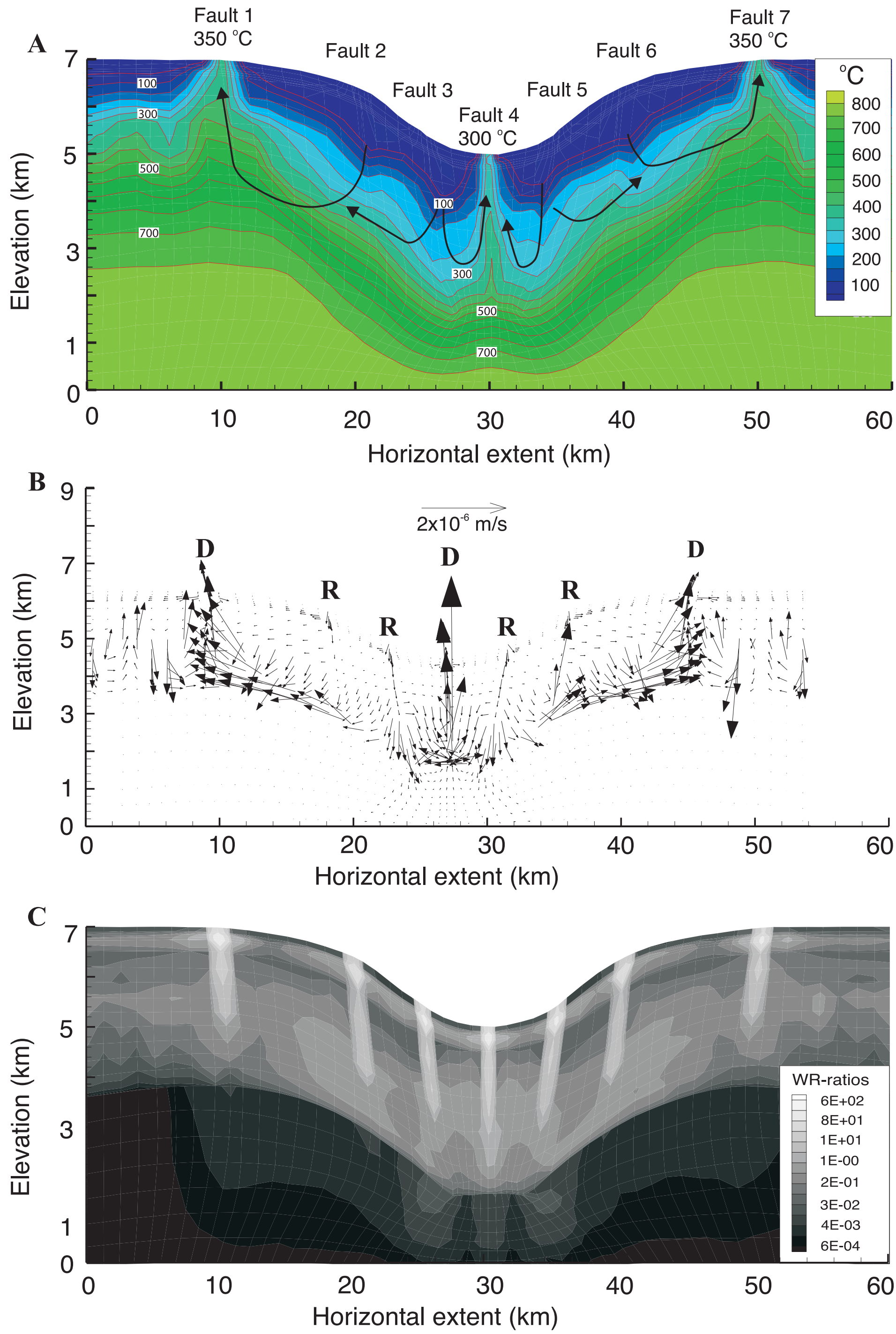

Fig. 3. Snapshot of (A) heat distribution, (B) fluid flow, and (C) cumulative water-rock ratios after 10,000 years for average conditions (average rock and fault permeabilities, see table 3) in the Lau Basin. Main fluid recharge occurs through faults 2, 3, 5, and 6 in the topographic depression. The outermost faults 1 and 7 experience significant fluid discharge, while fault 4 is only active at lower rock permeabilities. Cumulative water-rock ratios suggest most intense fluid flow occurs within and around faults as well as within the breccia zone and sheeted dike layer. Note that shown temperature distribution reflects conditions after 10,000 years, where the hydrothermal system has started to cool down and does not necessarily show maximum discharge temperatures (compare with figs. 6, 8 and table 3). D—fluid discharge; R—fluid recharge.

TABLE 3

Comparison of numerical results from rock permeability analysis showing recharge and discharge faults, discharge temperatures, discharge fluid velocity, and discharge duration

	Rock permeability (m^2)	Fault permeability (m^2)	Discharge faults	Recharge faults	Discharge duration (years)[1]	Discharge velocity (m/s) (max/average)[2]	Discharge temperatures (°C)
Low rock permeability	Breccia zone $1.3x10^{-17}$ Andesite 10^{-18}	$1x10^{-13}$	1	3, 5	228100*	$2.2x10^{-7}/9.1x10^{-8}$	150-450
			2[3]		25000	$3.5x10^{-7}/1.9x10^{-7}$	150-400
			4		226300*	$3.8x10^{-7}/1.3x10^{-7}$	150-450
			6[3]		24100	$3.8x10^{-7}/1.8x10^{-7}$	150-400
			7		227300*	$1.8x10^{-7}/7.5x10^{-8}$	150-400
Average rock permeability	Breccia zone $1.3x10^{-16}$ Andesite 10^{-17}	$1x10^{-13}$	1	3, 5	228100*	$2.5x10^{-7}/9.9x10^{-8}$	150-400
			2[3]		15000	$4.8x10^{-7}/2.7x10^{-7}$	150-400
			4		216000*	$6.6x10^{-7}/9.1x10^{-8}$	150-350
			6[3]		15000	$4.6x10^{-7}/2.7x10^{-7}$	150-350
			7		228100*	$1.8x10^{-7}/7.6x10^{-8}$	150-400
High rock permeability	Breccia zone $1.3x10^{-15}$ Andesite 10^{-16}	$1x10^{-13}$	1	3, 4, 5	164700	$8.9x10^{-7}/2.9x10^{-7}$	150-300
			2[3]		10600	$1.1x10^{-6}/6.8x10^{-7}$	150-400
			6[3]		15500	$9.6x10^{-7}/6.5x10^{-7}$	150-350
			7		129700	$5.7x10^{-7}/2.2x10^{-7}$	150-400

Note: Rock permeability values for sediments, sheeted dike complex and layered gabbro were kept constant (refer to table 1).
[1] Defined as fluid discharge having temperatures ≥ 150°C.
[2] Average calculated from maximum and minimum recorded fluid velocity values for discharge temperatures ≥ 150°C.
[3] Fault turns from initial discharge into recharge fault.
* Discharge duration limited to 230,000 years due to boundary effect.

Rock Permeability

Although permeability has the most influence on fluid movement in porous media, it is often difficult to apply meaningful values due to a lack of available data, the enormous time spans that apply to hydrothermal systems, and processes that influence rock permeability such as metamorphism, diagenesis, or alteration. The influence of rock permeability on fluid discharge behavior and alteration patterns has been tested by considering three scenarios representative of low, average, and high rock permeability (table 3).

Low rock permeabilities ($10^{-17}/10^{-18}$ m^2) encourage high temperature discharge (up to 450°C) due to slower fluid velocities. This fluid discharge occurs at elevated topographic positions (faults 1 and 7; see fig. 2 for location) due to fluid migration along the basement topography. An increase in rock permeability of one order of magnitude causes discharge velocities to increase but temperatures to drop between 15°C and 70°C. The onset of hydrothermal fluid discharge shifts to an earlier point in the simulation process (as an example, 7,000 to 700 years in fault 6) as rock permeability increases. The relative duration of high-temperature fluid discharge is comparable for low to average permeability, but under high rock permeability conditions discharge temperatures decline earlier and the overall discharge duration decreases (see table 3). Significant hydrothermal fluid discharge ($T > 150$°C) lasts between 10,000 to about 25,000 years for the inner discharge faults (faults 2 and 6), while the outermost faults (faults 1 and 7) and the central fault 4 exhibit hydrothermal activity for much longer (>200,000 years; see table 3); at high rock permeability fault 4 becomes a recharge zone. This is due to the increase in fluid discharge velocities, enabling a more efficient cooling of the heater and reducing the life span of the hydrothermal system. Fluid velocities also increase as rock permeability increases (table 3).

Calculated water-rock ratios show a similar distribution under most conditions, except for high rock permeability, where elevated water-rock ratios within the andesite and breccia zone indicate intensified fluid flux. Water-rock ratios show highest water-rock interaction occurring in and around faults and the breccia zone; significant fluid flow is also observed within the sheeted dike layer and to a lesser degree in the andesite unit. Simulations were terminated after 500,000 years to account for a 'boundary effect', where fluids circulate against the impermeable side boundaries and are eventually redirected to the outermost faults 1 and 7 after about 230,000 years; maximum discharge duration has therefore been set to 230,000 years. However, this aspect is not crucial for the sensitivity analysis or the interpretation of the overall modeling results.

Porosity and Thermal Conductivity

Although porosity and permeability usually exhibit a positive correlation in porous and fractured media, this is not always the case, as for example in volcanic rocks (Ingebritsen and Sanford, 1998). Changes attributed to thermal conductivity may be expected in areas where heat is transmitted primarily by conduction rather than convection, as is the case away from faults; this factor may also vary as a function of the size and geometry of the numerical model. To investigate the influence of porosity and thermal conductivity, simulations have been run with either minimum or maximum values (table 2) relative to average data for the volcanic packages only (see table 1). Results predict no significant changes for either heat distribution or fluid flow except for the central fault 4, which at low porosity does not exhibit fluid discharge and fault 5, which experiences short fluid discharge at elevated thermal conductivity values. Since these deviations are local phenomenon, it is concluded that porosity and thermal conductivity do not greatly influence the hydrothermal convection scheme in this model. Computer modeling with a different, more detailed finite element model of an ancient seafloor hydrothermal system however, has shown that changes in porosity or thermal conductivity can have pronounced effects on the overall system behavior (Schardt and others, 2005).

Faults

The importance of synvolcanic faults in facilitating fluid flow and heat exchange between the heat source and host rocks to form characteristic alteration patterns and massive sulfide deposits has long been recognized. Focussed fluid flow along growth faults is a major mechanism for the transport of hot, metalliferous fluids to the seafloor, as seen in the black and white smoker chimneys frequently encountered in submarine settings (Franklin and others, 1981; Lydon, 1988; Stanton, 1991; Large, 1992; Lydon, 1996; Curewitz and Karson, 1997). To assess the influence of certain fault properties, a number of simulations have been performed to investigate several fault parameters.

Fault distribution.—To determine how fault spacing, extension, and distribution affect fluid flow patterns, faults shown in figure 2 are successively activated. A fault is considered to be active when it is given a permeability greater than the surrounding rocks. With three faults activated, a simple recharge-discharge regime develops where the central fault 4 acts as a recharge zone while the outer faults (2 and 6) show fluid discharge with venting temperatures of $\sim$200°C and fluid velocities of $\sim 2 \times 10^{-7}$ m/s (figs. 4A and 5A). With five faults the main fluid discharge switches to the outer faults while faults 2 and 6 record less hydrothermal activity.

Simulations with all seven faults activated show additional fluid discharge from the central fault 4 (figs. 4C and 5C). This fault switches from initial recharge behavior to fluid discharge after about 14,000 years, presumably when sufficient heat from the magma chamber is extracted to produce buoyant hydrothermal fluids. While highest fluid velocities are predicted for fault 4, discharge temperatures are highest in the outermost discharge faults. Figure 5 also indicates that significant lateral fluid flow occurs in case B and C in the breccia zone and the sheeted dike-gabbro boundary. Significant fluid migration within the sheeted dike zone is attributed to the large permeability difference between the sheeted dikes complex (1×10^{-17} m^2) and the underlying gabbro unit (1×10^{-18} m^2) as well as higher temperatures within this rock layer compared to the andesite and breccia layer. This finding is supported by other studies, predicting fluid flow refraction between media of larger permeability differences and placing major fluid flow at the sheeted dike boundary (Sleep, 1991; Lowell and Burnell, 1991; Rosenberg and others, 1993). Other work suggests that the base of the sheeted dikes represents a major chemical reaction zone requiring significant fluid flow (Richardson and others, 1987; Varga and others, 1999).

Fault permeability.—Figure 6 shows discharge temperatures as a function of fault permeability and illustrates that increasing fault permeability has a selective effect for individual faults. While all faults are predicted to exhibit fluid discharge at some point during calculations, faults 1 and 7 are the main locations of fluid discharge under all conditions with faults 3, 4, and 5 showing intermitted fluid discharge; other faults are much less hydrothermally active (see fig. 6 for explanation). Differences in discharge temperatures, fluid velocity, and discharge duration between opposing faults relative to the magma chamber are attributed to small geometric irregularities in numerical grid construction, causing slightly different flow patterns and fluid characteristics. These differences however have no impact on the overall evolution of the hydrothermal system.

The outermost faults (faults 1 and 7) record similar discharge temperatures, while faults 2 and 6 show somewhat lower discharge temperatures at elevated fault permeability; under initial (average) rock permeability conditions the central fault 4 records

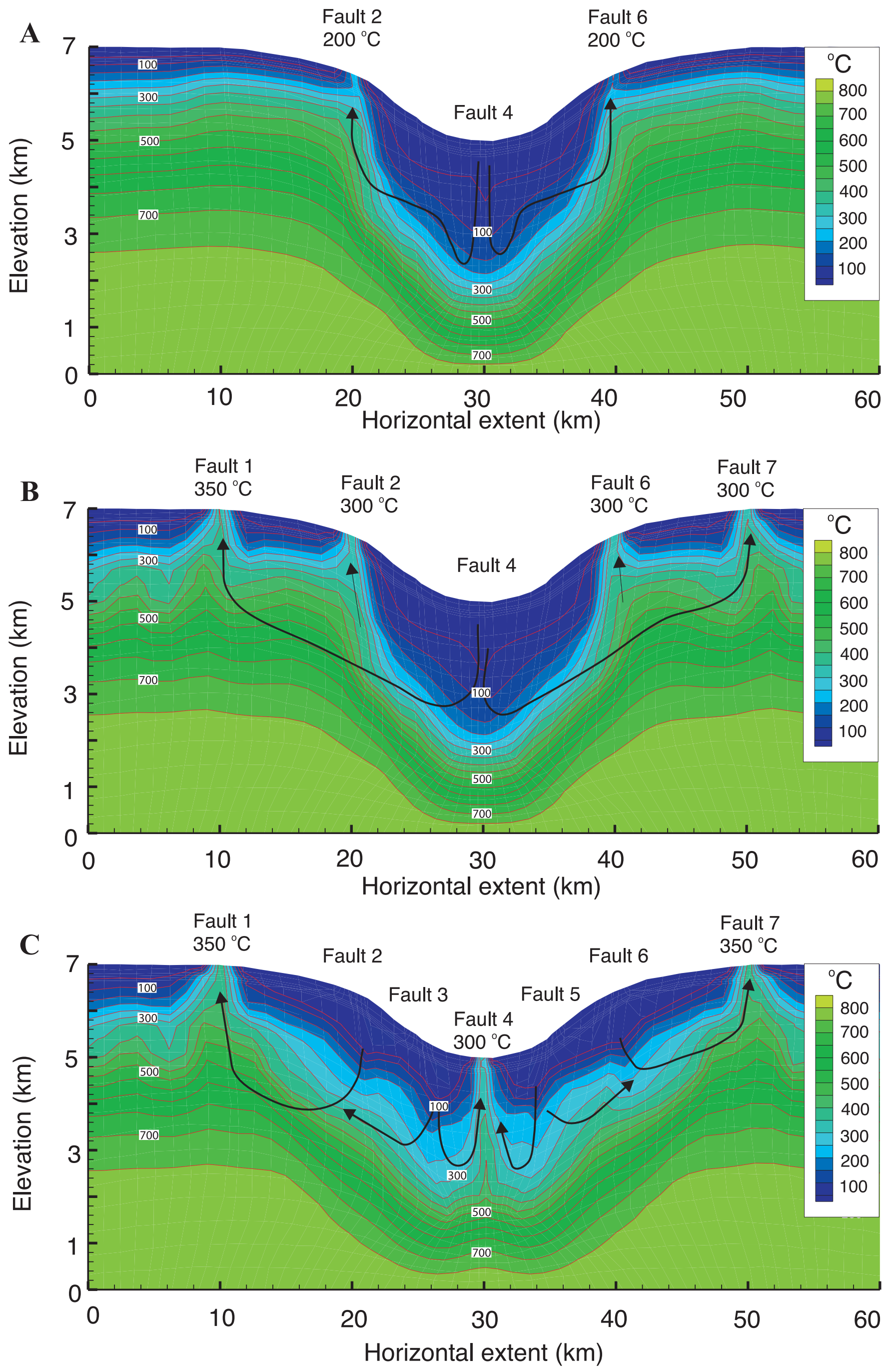

Fig. 4. Temperature distribution for simulations with different fault setups: (A) three faults, (B) five faults, and (C) seven faults after 10,000 years. In all cases, major fluid discharge occurs at elevated topographic positions as well as through fault 4 directly overlying the magma chamber, while fluid recharge is concentrated on the slopes of the depression. Note that discharge temperatures reflect conditions after 10,000 years while maximum discharge temperatures of individual faults may be higher during the lifespan of the hydrothermal system.

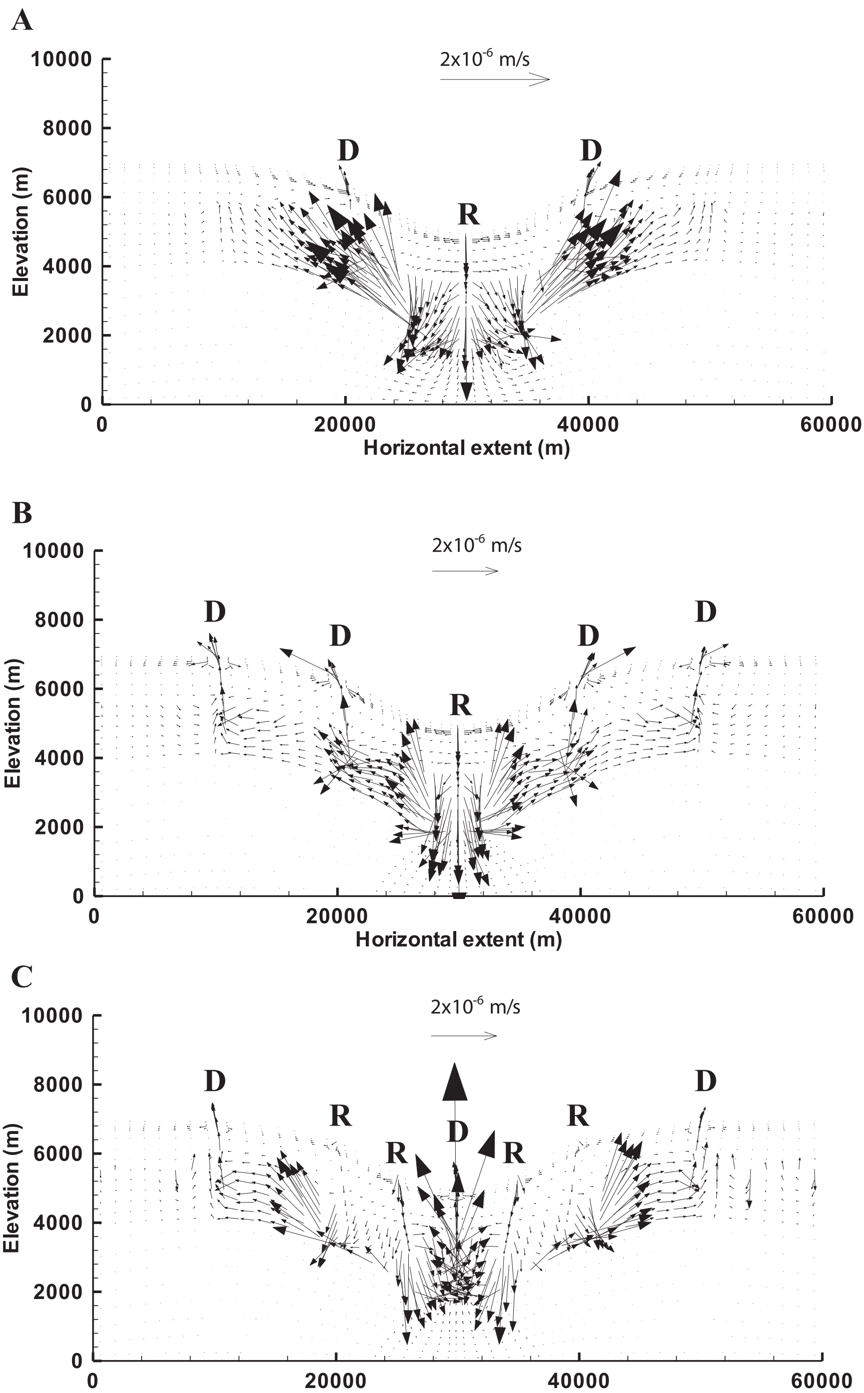

Fig. 5. Fluid flow velocity and distribution patterns for different fault setups: (A) fault 2, 4, and 6, (B) fault 1, 2, 4, 6, 7, and (C) all faults after 10,000 years. Major fluid flow occurs within the breccia zone as well as the sheeted dike-gabbro boundary due to the large permeability difference between the two units (one order of magnitude). D—fluid discharge; R—fluid recharge.

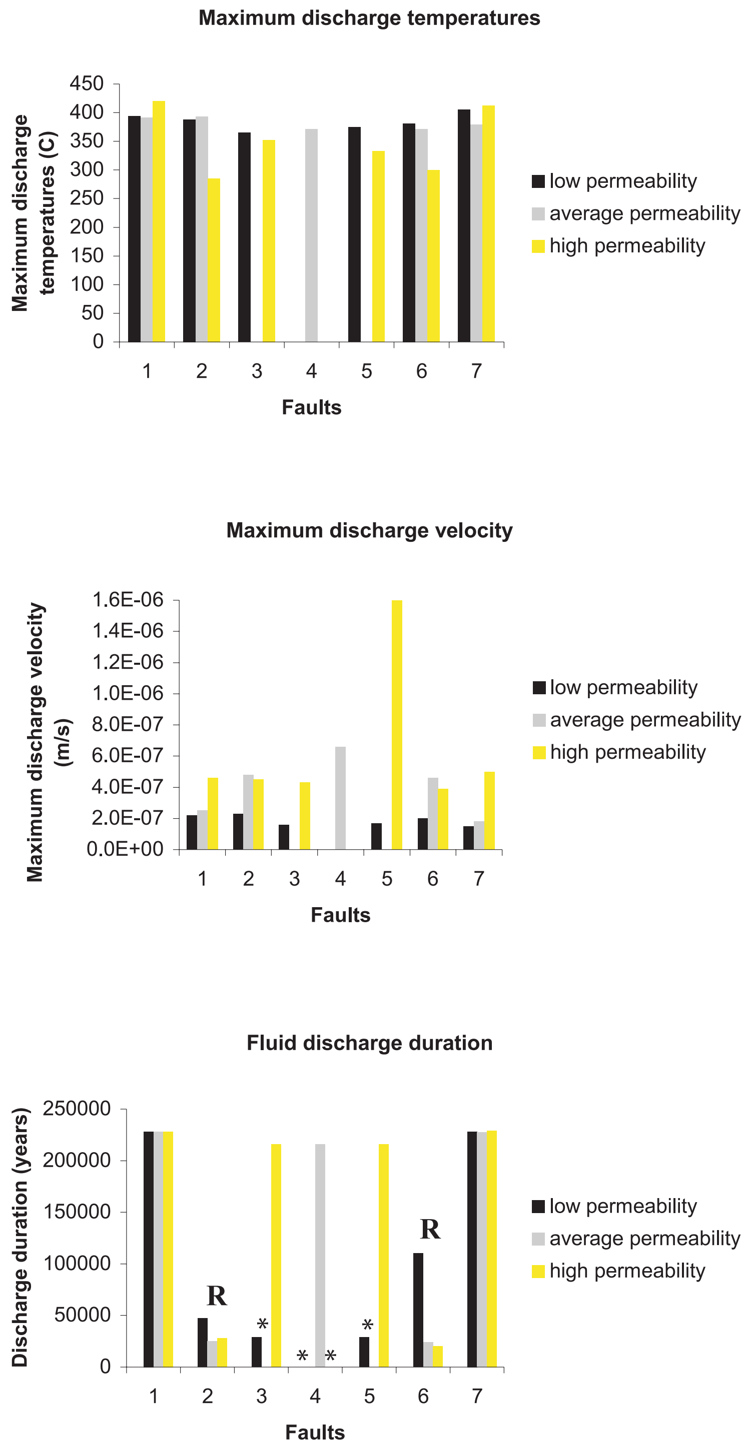

Fig. 6. Summary of fluid discharge temperatures, velocity, and discharge duration as a function of fault permeability at average rock permeability (see table 3). The end of discharge duration has been set to 230,000 years for faults 1 and 7 due to the 'boundary effect' (see text for explanation). Note that compared to faults 1 and 7, all other faults show less activity under the range of permeabilities investigated; they instead act as recharge zones and/or show little fluid discharge, low permeability = 2.5×10^{-15} m^2, average permeability = 2.5×10^{-14} m^2, high permeability = 2.5×10^{-13} m^2; R—mostly fluid recharge, *—no predicted fluid discharge.

fluid discharge only at average fault permeability. Other faults previously acting as pure recharge areas (faults 3 and 5) also become zones of fluid discharge due to the permeability increase. Fluid discharge temperatures are generally highest at lower fault permeabilities since low fault permeability slows fluid recharge and the heat source is cooled less efficiently. The elevated discharge temperature in faults 1 and 7 under these conditions is short-lived and attributed to shifting convection patterns.

In general, fluid velocities exhibit a significant increase at high fault permeability and a shift of hydrothermal heat and fluid flow from regions surrounding the heat source to peripheral areas, implying a more effective heat removal and increased fluid mobility. Elevated fault permeability shifts fluid discharge patterns rather than intensifying discharge temperatures in established discharge faults. These results indicate that changing fault permeabilities alter the general hydrothermal convection scheme from a recharge-dominated system (four recharge faults vs. three discharge faults) at average fault permeability to a discharge-dominated hydrothermal system (four discharge faults vs. three recharge faults) at high fault permeability. Discharge duration for faults 1 and 7 are unaffected by changes in fault permeability, while the central faults (faults 3, 4, and 5) show prolonged hydrothermal activity (>200,000 years) at elevated fault permeability.

It is also of interest in this regard to examine the case when a single fault has a higher permeability compared to other faults. To test this, a simulation was run where the central fault 4 has been set to twice the permeability (5×10^{-14} m^2) compared to all other faults (2.5×10^{-14} m^2). Results for this scenario are interesting since they indicate an unexpected change in the hydrothermal convection scheme (fig. 7A). While outer faults show no noticeable changes, faults 3 and 5 switch from recharge to discharge and fault 4 becomes a recharge zone. Our explanation for this behavior is that in this model an initial higher permeability in fault 4 encourages and maintains additional fluid recharge and thus prevents the switch from recharge to discharge; this in turn causes faults 3 and 5 to respond accordingly and switch to fluid discharge. To see whether this is a special case, and applies only to fault 4 due to its location, fault 3 was assigned a higher permeability (5×10^{-14} m^2). Figure 7B shows that a higher permeability for fault 3 does not have a significant effect on either fault 3 and 5 (recharge zones) or the central fault 4 (discharge fault). Hydrothermal convection patterns remain and the initial recharge-discharge pattern is maintained. This behavior is attributed to the basement topography, which forces fluid recharge through faults 3 and 5, independent of permeability changes or the proximity of the heat source.

While the true permeability of fault zones is poorly known, larger fault permeability differences between faults 3, 4, and 5 (up to one order of magnitude) show similar results. In addition, results involving higher values ($>5 \times 10^{-13}$ m^2) show little difference at lower rock permeabilities or cause numerical instabilities at higher rock permeability due to computational limits.

DISCUSSION

Submarine Hydrothermal Heat and Fluid Flow

The predicted fluid transport and hydrothermal activity in the Lau Basin model is controlled by the model geometry and rock permeability, producing distinct areas of fluid recharge and discharge. The following section considers the main processes of the hydrothermal system and their relation to the main simulation results.

Heat Flow

Heat transport results from the generation of buoyancy-induced thermal gradients producing a hydrothermal convection regime where heat is extracted from the

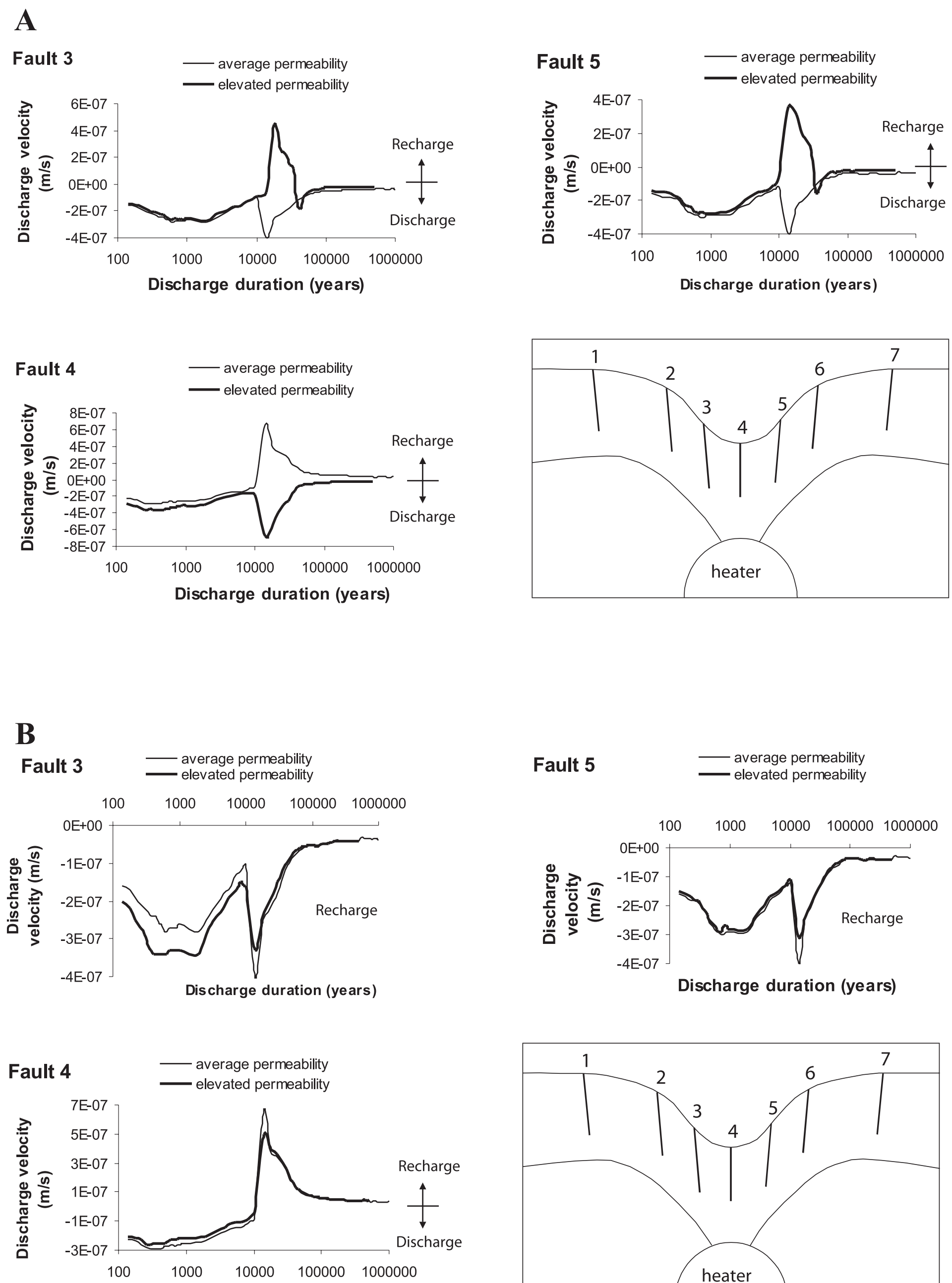

Fig. 7. (A) Fluid velocities and discharge behavior for higher permeability of fault 4 (5×10^{-14} m^2); other faults have average permeability (2.5×10^{-14} m^2). A shift to fluid recharge is predicted to occur after ~10,000 years for fault 4, probably due to the stabilization of fault 4 as a recharge fault and the consequent fluid discharge through neighbouring faults. (B) Fluid velocities and discharge behavior for higher permeability of fault 3 (5×10^{-14} m^2); other faults have average permeability (2.5×10^{-14} m^2). A higher permeability of fault 3 predicts no shift in discharge/recharge behavior, which suggests that fault 3 and 5 are favored as zones of fluid recharge due to the nature of the basement topography.

central intrusion and transferred chiefly within the volcanic rock zones and sheeted dike layer towards topographic highs. Within the volcanic rocks, temperatures reach about 400°C and increase to about 600°C in the dike complex and layered gabbro unit. Overall predicted fluid discharge temperatures range from 150°C to 450°C and major fluid discharge occurs within the outer faults and the region overlying the magma chamber. Discharge temperatures are in agreement with measured vent temperatures in the Lau Basin (334°C to >400°C; Charlou and others, 1990; Fouquet and others, 1991; Von Stackelberg and Von Rad, 1994) and exit temperatures are controlled mainly by permeability differences (fig. 8A). Lower discharge temperatures (up to 350°C) are predicted at elevated rock and fault permeability since fluids are circulating rapidly and are not as effective in removing heat from the magma chamber. While the distribution of faults does not alter discharge temperatures, it does affect discharge duration: significant fluid discharge ($T \geq 150$°C) with three faults lasts for ~229,000 years for faults 2 and 6, while with five faults activated, only ~100,000 years of activity are recorded for the same faults, since heat is removed more effectively from the magma chamber. No significant changes have been observed when other rock properties such as porosity or thermal conductivity are altered.

Fluid Flow

Fluid discharge velocities depend primarily on fault permeability and to a lesser degree on rock permeability (fig. 8B). Highest discharge velocities (1.6×10^{-6} m/s) are predicted at elevated fault and rock permeability and fluid velocities drop to $<1 \times 10^{-8}$ m/s as permeabilities decrease. Although these values are significantly lower than those reported from modern seafloor hydrothermal systems (>1 m/s; Converse and others, 1984; Ginster and others, 1994) modeled fluid exit velocities apply to the assigned surface area of the fault in the model section (400 m × 1,100 m) rather than a typical seafloor chimney orifice (~3 cm to >30 cm; Cann and others, 1985, 1986). The width of the faults (400 m) was chosen partially due to constraints of the modeling software, which requires a certain low order fault/rock permeability ($<10^{-13}/10^{-14}$ m^2), to enable convergence of heat and fluid transport with a high-temperature heat source and selected grid spacing. However, model fluid velocities may be compared to vent discharge velocities by relating them to similar surface areas. Because volume flow rate is the same regardless of cross-sectional area or velocity, we use the relationship:

$$A_1 v_1 = A_2 v_2 \tag{1}$$

where A_1 and v_1 are the surface area and fluid velocity of the model (fault surface area) and A_2 and v_2 are the surface area and the fluid flow of the vent. For a vent orifice of 10 × 10 cm, model velocities of 1×10^{-7} m/s predicted from the model convert to exit velocities of 4.4 m/s, which compares well with exit velocities observed on the seafloor (>1 m/s, Converse and others, 1984; Ginster and others, 1994). Lower temperature discharge regions observed in the Lau Basin measure about 100 × 100 meters (Fouquet and others, 1991) and model fluid velocities for this type of diffusive fluid discharge are about 1×10^{-4} m/s.

The fluid velocity conversion also allows an estimate of the heat flux from a single discrete vent, which can be calculated by applying the formula from Lowell and Germanovich (1994) assuming the same vent size (10 × 10 cm):

$$Q = \rho_f c_f v(T - T_0)\pi d^2/4 \tag{2}$$

where ρ_f is the fluid density, c_f is the specific heat of the venting fluid, v is the fluid velocity for a 10 × 10 cm vent, T and T_0 are the temperatures of vent and of ambient seawater respectively, and d is the vent width. Results yield heat flux values between 1.8 and 21 MW for a range of temperatures (300°C–400°C) and converted fluid velocities

A

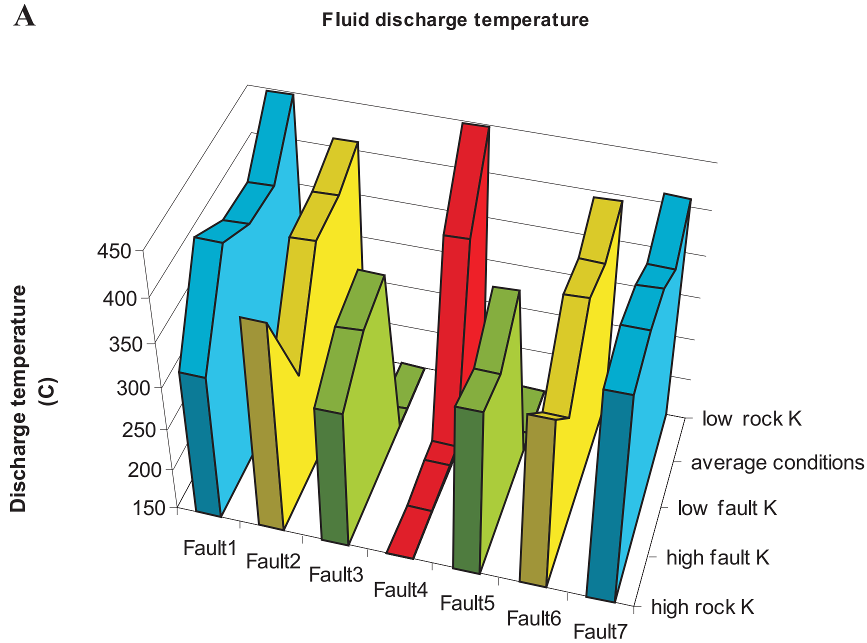

B

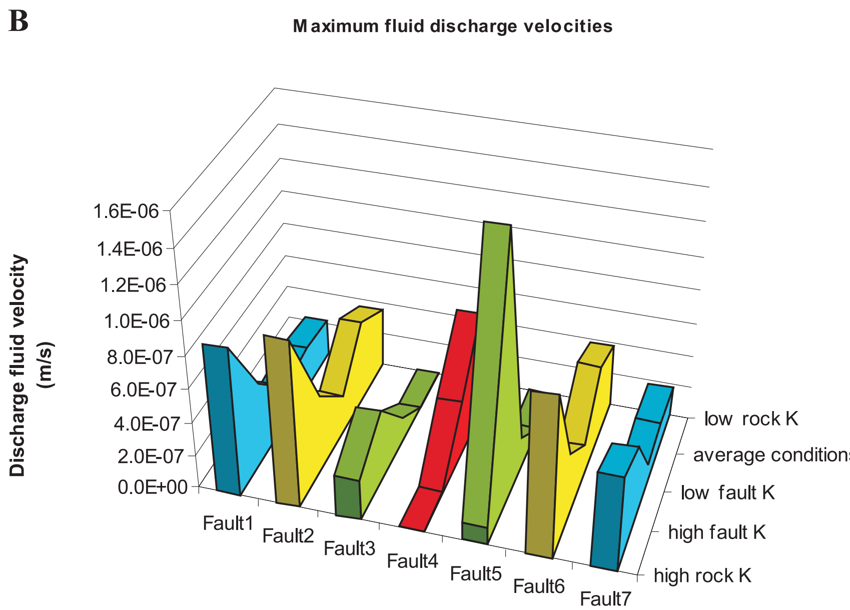

Fig. 8. Summary results for (A) fluid discharge temperatures and (B) fluid discharge velocity distribution as a function of rock and fault permeability. (A) Low permeabilities predict highest discharge temperatures (450°C) for the outer faults 1 and 7 and fault 4, which decrease as rock and fault permeability increase. A change in the hydrothermal recharge-discharge regime is predicted to occur at elevated permeabilities: fault 4 ceases fluid discharge and instead faults 3 and 5 are predicted to vent lower temperature fluids (350°C). Graph B emphasizes the control of fault and rock permeability of hydrothermal fluid discharge through individual faults.

(4.4 to 44 m/s) obtained from simulation results. These values compare well with data reported by Lowell and Germanovich (1994), which range from 1 MW to several tens of MW for single vents and values measured for submarine hot springs on the East Pacific Rise by Converse and others (1984), which range from 0.5 to 250 MW.

Water-Rock Interaction and Alteration

The general distribution patterns of water-rock ratios for the Lau model are similar for all simulations: highest water-rock ratios (~600) occur around faults and to a lesser extent within the breccia zone and the sheeted dike/andesite region. Elsewhere, water-rock ratios are much lower (0.1–3) and compare well with values calculated by Spivack and Edmond (1987) for hydrothermal fluids at high temperatures (0.28–3) and calculated water-rock ratios from various geochemical and numerical modeling studies (<1 to 50—Mottl, 1983; ~1.4—Cann and others, 1985/1986; <0.1 to 24—Fisher and Narasimhan, 1991). These patterns directly reflect the permeability distribution in the system and underlines faults and high-permeability rock units as the predominant fluid flow pathways. In addition, simulation results predict significant fluid flow and elevated water-rock ratios at the boundary between units of large permeability differences as in the case of the sheeted dike layer and the gabbro unit (fig. 9).

The temperature distribution, water-rock ratio and hence alteration zonation modeled here are in general agreement with alteration patterns found on the seafloor, where low temperature (<200°C) regions beneath the surface correspond to zeolite facies alteration (Alt and others, 1985; Gillis and Robinson, 1988). With increasing depth in the andesite layer, predicted temperatures reach up to 400°C, equivalent to chlorite alteration (Alt and others, 1986, 1998) and in the sheeted dike section temperatures >400°C equate to amphibolite facies alteration (Galley, 1993; Alt, 1995). These broad alteration zones are disturbed near fault regions, where hydrothermal fluids are focussed and highest water-rock ratios occur, indicative of intense water-rock interaction. These areas are interpreted to represent chlorite alteration and sericitization due to focussed flow of hydrothermal fluids as observed in ophiolites and mid-ocean ridge environments (Alt and others, 1998).

Life Span of the Hydrothermal System

The duration of the hydrothermal system and associated fluid discharge modeled here is dominated by off-axis faults at topographic highs (fig. 10). High temperature fluid discharge ($T > 150°C$) can last from 2,000 to ~90,000 years for faults 2 and 6 and >200,000 years for all other faults. This time span is comparable to results by Cathles and others (1997) who estimated that hydrothermal fluid discharge with temperatures >200°C can last between 100,000 years and about 800,000 years depending on host rock permeability. Other factors that may influence the discharge behavior and venting duration of the Lau Basin model include changing boundary conditions, such as allowing fluids to enter or leave the system on the sides (Schardt, ms, 2004). Faults 1 and 7 are generally the hydrothermally most active faults and the most likely location for the formation of massive sulfide deposits. While other faults can also show significant hydrothermal activity, they usually don't exhibit coinciding elevated discharge temperatures and fluid velocity (faults 3 to 5) or their discharge duration is insignificant compared to faults 1 and 7 (faults 2 and 6, compare figs. 8 and 10).

In the context of a modern seafloor setting, such as the back-arc seafloor-spreading center hosting the Lau Basin, significant fluid discharge can be expected in off-axis regions on the flanks of grabens or other tectonic highs, such as the Valu Fa Ridge, which flanks the Lau Basin (Fouquet and others, 1993; Herzig and others, 1993, 1998; see fig. 1). This relationship is also supported by seafloor observations and other

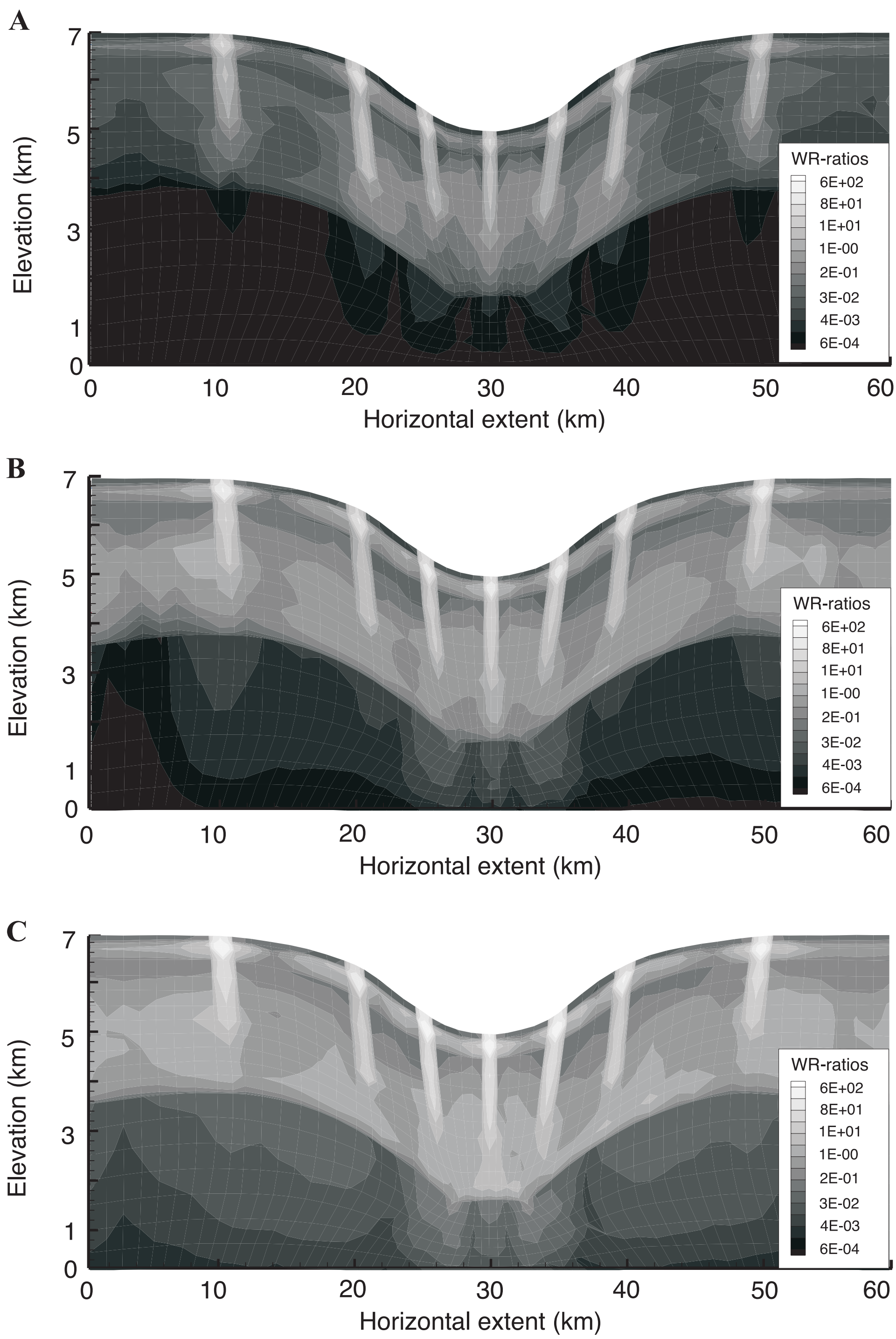

Fig. 9. Development of cumulative water-rock ratios as a function of hydrothermal fluid flow. (A) Early in the life of the hydrothermal system (1,000 yrs), most fluid flow occurs near the heater and within nearby faults as recharging fluids are heated and start to convect. (B) At 50,000 years hydrothermal fluid flow has spread to the outer faults and significant fluid migration is predicted to occur within the breccia zone and sheeted dike zone. At this point fluids also begin to penetrate into the clearly distinguished low-permeability gabbro unit and the sides of the heat source. (C) After 500,000 years there is widespread fluid migration in most of the system, especially directly above the heat source, as the hydrothermal system penetrates deeper into the freezing magma chamber.

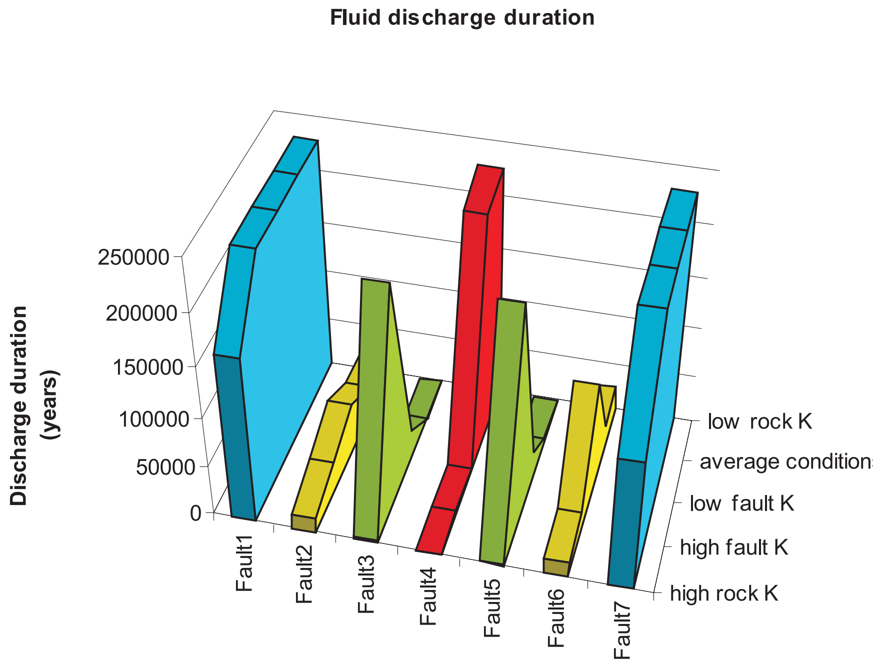

Fig. 10. Hydrothermal fluid discharge duration for the Lau Basin model. Most fluid discharge occurs through the outermost faults under all conditions. At lower permeabilities, fault 4 also exhibits significant fluid discharge, whereas all other faults are insignificant with regard to fluid discharge; they are the predominant recharge zones.

theoretical calculations (Lowell, 1980; Green and others, 1981; Davis and others, 1989; Fisher and others, 1994; Davis and others, 1996).

The Lau Basin Hydrothermal System and Massive Sulfide Ore Body Formation

A conceptual model of the evolution of the Lau Basin submarine hydrothermal system and the formation of VHMS deposits is shown in figure 11, where deposit formation in oceanic crust is represented by a slow-spreading, sediment-covered ridge setting. Conclusions for the evolution of the hydrothermal system are based on previous theoretical studies, models, and modeling results (Lowell, 1980, 1991; Lowell and Burnell, 1991; Lentz, 1998; Schardt, ms, 2004; Schardt and others, 2005), as well as this study:

Early in the life of the rifting process rock and fault permeabilities are likely to be high due to the young age of the crust and the creation of fault structures associated with the production of new crust (Sinton and Detrick, 1992; fig. 11A). Fluid flow patterns show intense fluid circulation within the most permeable rock units (commonly breccia zone) as well as in the sheeted dike layer and major fluid migration occurs via the major syn-rift fault system. Fluid discharge occurs directly above the heat source and at elevated topographic positions, with fluid recharge sites located on the flanks. There is also lateral fluid flow occurring within the upper part of the stratigraphy and along the sheeted dike—gabbro boundary, channelling fluids to more remote off-axis faults. This agrees with predictions of previous studies, which argued for significant fluid flow in the deeper portion of oceanic crust, within the sheeted dike layer (Lowell and Burnell, 1991; Sleep, 1991; McCollom and Shock, 1998; Lowell and others, 2003). High discharge fluid velocities are predicted for faults in the rift axis in

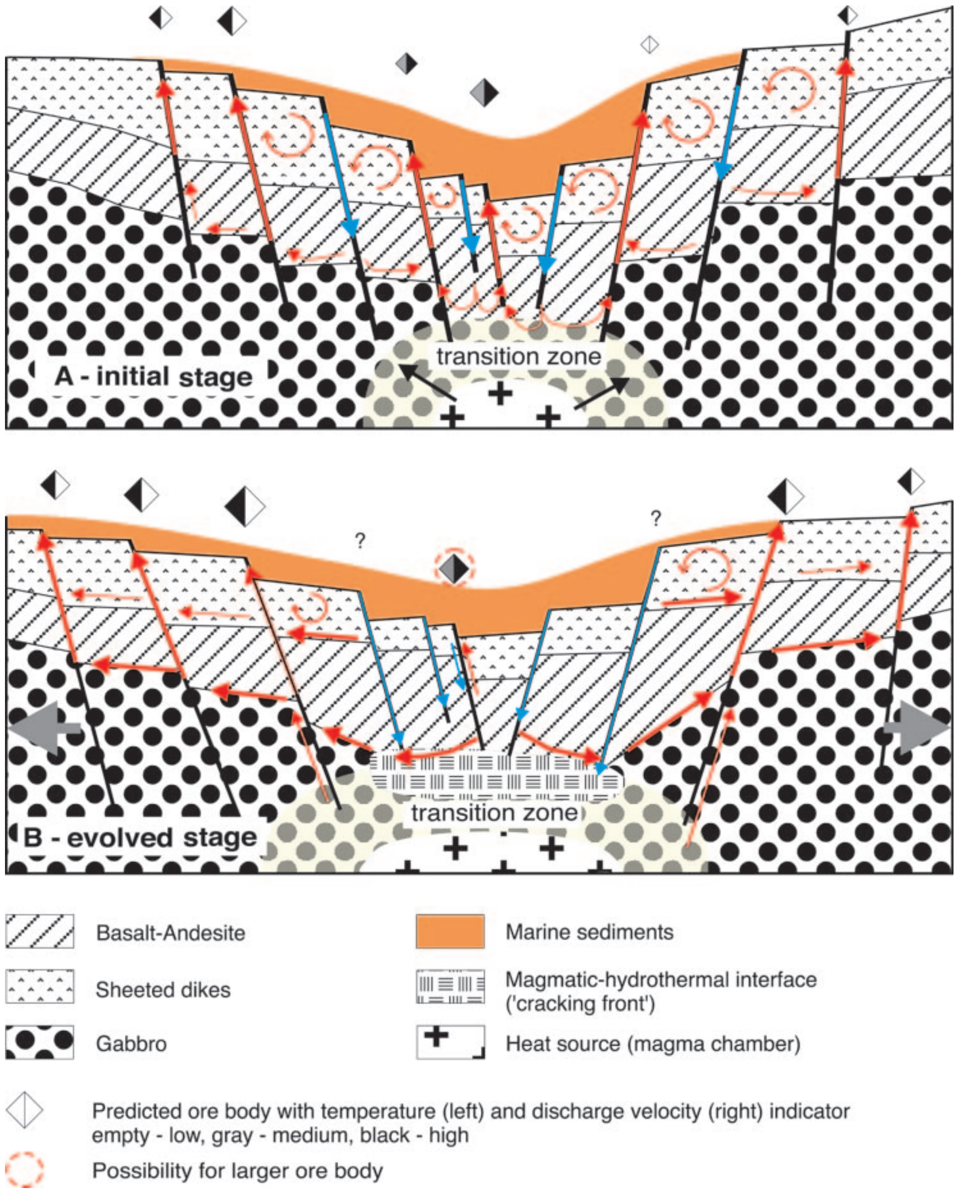

Fig. 11. Proposed evolution of Lau Basin hydrothermal system with regard to heat and fluid flow. (A) The initial stage is characterized by high fault permeabilities allowing the establishment of a hydrothermal convection scheme, which is determined by fault spacing. Major hydrothermal fluid discharge is expected to occur above the heat source but more distal off-axis faults also experience significant fluid flux. (B) As the rift system evolves, the hydrothermal system transforms into a central recharge zone with major fluid discharge occurring at more distant fault locations. This suggested change is caused by the penetration of the hydrothermal convection system into the top of the heater, establishing a transition zone (not modeled), which to some extent controls the fluid migration along basement topography. Overall, the largest VHMS deposits are expected to form at off-axis topographic elevated positions depending on the depth of the heat source and the permeability history of individual faults. Significant massive sulfide deposition may also occur above the magma chamber especially if the boundary zone is repeatedly disturbed by magmatic activity. Size of diamonds show relative size/amount of accumulated massive sulfides calculated from modeling results and location and type of shading refers to discharge temperature and velocity based on modeling results (long-lasting, high-temperature fluid discharge at individual faults). Sites of high temperature fluid discharge (black triangle left) are expected to show a larger percentage of high-temperature ore mineralogy (for example, high amounts of chalcopyrite) compared to lower-temperature discharge locations, which will be sphalerite-galena rich or simply pyrite.

the vicinity of the magma chamber, since these fluids have the shortest migration path and experience the largest buoyancy forces. Off-axis faults have lower discharge velocities but higher discharge temperatures, since the fluids migrate further through the subsurface and are not continually exposed to cold, recharging seawater. The general recharge–discharge pattern at this stage depends primarily on fault spacing, that is the position of individual faults relative to the magma chamber. Discharge temperature and velocity distribution are controlled by the relative distance of off-axis faults from the magma chamber.

As the rift basin evolves, the hydrothermal system expands. Fluid flow penetrates deeper, into the outer zone of the magmatic intrusion due to thermal cracking of overlying rocks, and establish a transition zone at the magmatic–hydrothermal interface comparable to the 'thermal cracking' front (not modeled here) of Lister (1972), Cathles (1983) or Barrie and others (1999a, 1999b; fig. 11B). This process is suggested to transform the hydrothermal convection pattern from an alternating recharge–discharge pattern to a large, central recharge zone with distinct peripheral off-axis discharge regions. Although permeability changes as a function of time are not directly modeled here, simulations with different permeabilities and earlier results (Schardt, ms, 2004) support the establishment of this recharge zone by the drawdown of seawater, which causes cooling and would result in a decrease in fault and rock permeability due to thermal shrinkage and the precipitation of minerals such as amorphous quartz and anhydrite as demonstrated by Lowell and Yao (2002) and Lowell and others (2003). While this process may not be pervasive throughout, it is suggested to force fluids to travel along basement highs to off-axis hydrothermal discharge sites well removed from the heat source. Simulation results predict that these off-axis faults are now the sites of major hydrothermal fluid discharge due to their distance from the main recharge zone. This in turn may isolate fluid flow pathways from rapid cooling and hydrothermal discharge may be sustained for a long time; this fluid flow pattern is also supported by field observations (Fouquet and others, 1993). Depending on the rock lithology, permeability distribution, and depth and nature of the heat source, major hydrothermal fluid discharge is also predicted to occur above the axial magma chamber as shown in figures 8 and 10. However, due to the central location of the predicted recharge zone, it is argued here that discharging fluids may show lower temperatures and the resulting massive sulfide accumulation might be less significant compared to the total ore deposition at elevated off-axis topographic positions depending on the magmatic-tectonic activity of the system.

Ore body formation.—Three types of discharge fluids can be distinguished based on numerical simulation results: high temperature fluids ($>370°C$), high velocity fluids ($>1 \times 10^{-6}$ m/s), and low temperature/low velocity fluids (see diamonds in fig. 11). While predicted ore mineralogy, reflected by the relative amounts of high-temperature and lower-temperature ore minerals, is a function of simulated discharge temperature, the size of individual deposits will also depend on the overall fluid velocity and the projected discharge duration, based on modeling results.

Numerical simulations from the Lau Basin model produce detailed records of temperature evolution and fluid flow development for individual faults as a function of time, which can be used to calculate the size of potential ore bodies at different fault locations (Schardt, ms, 2004):

$$m_{\text{ore body}} = \sum\left[\frac{(V_{cell}*v*\rho_f*t_{step}*m_{Zn+Cu})}{1E+6}\right]*x \tag{3}$$

where V_{cell} is the volume of discharging fluid corresponding to an appropriated convection cell for a single time step, v is fluid velocity, ρ_f is fluid density, t is time step, m_{Zn+Cu} is the combined mass of transported base metal in ppm, and x is metal

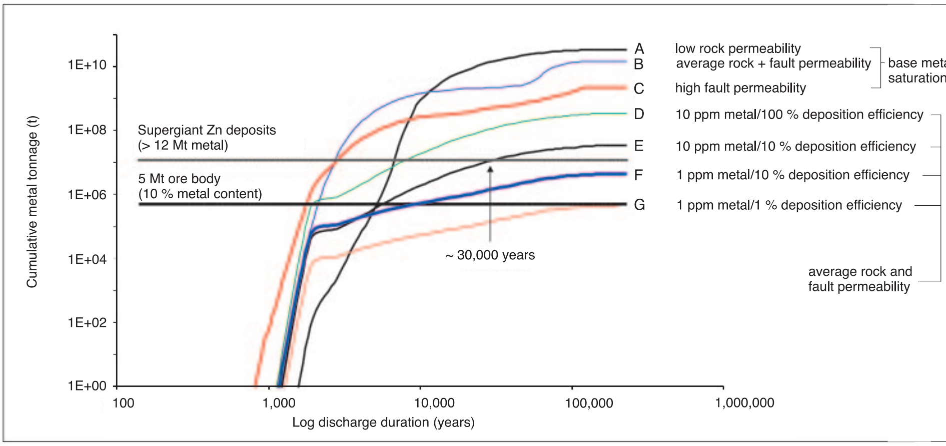

Fig. 12. Cumulative metal tonnage of predicted ore deposit formation as a function of rock properties, fluid properties, and discharge duration. Under most conditions (lines A to E) a significant ore body (5 Mt with 10% base metals) may form in less than 6,000 years, depending on the metal content and deposition efficiency. A fluid with a 1 ppm base metal content and a 10 percent deposition efficiency (line F) would take about 10,000 years to accumulate enough metal while fluids with less deposition efficiency (line G) will be unable to form a significant ore body. To form a supergiant ore body (>12 Mt of total metal) in <10,000 years, hydrothermal fluids either require greater than 10 ppm base metal and/or more than 10 percent deposition efficiency, since a 10 ppm/10% deposition efficiency fluid (line E) takes about 30,000 years to accumulate enough base metal. See table 4 for a list of the conditions of each case.

deposition efficiency. Dividing results by one million and multiplication by x yields metric tons of accumulated base metals over time; metal solubility data for Zn and Cu were taken from Ohmoto and others (1983) and Huston and Large (1987). To obtain the amount of fluid available to form a deposit the minimum size of the corresponding convection cell is calculated assuming that fluids circulating within this rock volume contribute to the precipitation of base metals by some focussing mechanism, such as at the intersection of crosscutting fault planes. These estimates are then used to compute the total amount of fluids available to form an ore deposit, based on discharge temperatures >150°C. This cut-off value is based on the solubility of major ore-forming sulfide minerals, which reach significant metal concentrations in the fluid (>1 ppm) above 150°C (Large, 1992).

To illustrate the potential for ore body formation as predicted by numerical simulation results, fault 7 has been chosen. Fault 7 is situated at an elevated topographic position and exhibits a high potential for ore deposition in terms of its hydrothermal history as well as location (Fouquet and others, 1993; Herzig and others, 1993). Figure 12 plots the cumulative amount of base metals (Zn + Cu) for a number of scenarios as a function of hydrothermal evolution against a 5 Mt ore body with a 10 percent base metal content as well as a supergiant deposit (>12 Mt total metal) as defined by Singer (1995). All calculations are carried out without lead, since very little lead is found in hydrothermal fluids on the seafloor in general (Von Damm, 1995) and in hydrothermal fluids of the Lau Basin in particular (Fouquet and others, 1993); table 4 lists conditions for each case shown in figure 12 along with the formation time.

Timing of ore body formation.—A significant ore body (5 Mt with 10% base metals) is predicted to accumulate in about 1,000 to ~6,000 years under most conditions (case A to E in fig. 12; see also table 4). The world average VHMS deposit size is 17 Mt at 8.4 percent base metal (Large and Blundell, 2000; R. Large, 2004, personal communication). If emerging fluids carry only a maximum of 1 ppm of base metal (line F; fig. 12)

TABLE 4

Summary of modeling conditions for calculated ore deposition for different cases shown in figure 12

Case	Rock permeability (m^2) Breccia Zone Andesite	Fault permeability (m^2)	Metal in solution (ppm)	Deposition efficiency (%)	Time to form 5 Mt/Supergiant deposit (years)
A	low ($1.3x10^{-17}$, 10^{-18} m^2)	$2.5x10^{-14}$	saturation	100	5,000/6,500
B	average ($1.3x10^{-16}$, 10^{-17} m^2)	$2.5x10^{-14}$	saturation	100	2,000/3,000
C	average ($1.3x10^{-16}$, 10^{-17} m^2)	$2.5x10^{-13}$	saturation	100	1,800/3,000
D	average ($1.3x10^{-16}$, 10^{-17} m^2)	$2.5x10^{-14}$	10	100	2,000/8,200
E	average ($1.3x10^{-16}$, 10^{-17} m^2)	$2.5x10^{-14}$	10	10	5,500/30,000
F	average ($1.3x10^{-16}$, 10^{-17} m^2)	$2.5x10^{-14}$	1	10	9,100/never
G	average ($1.3x10^{-16}$, 10^{-17} m^2)	$2.5x10^{-14}$	1	1	never/never

results predict that with a 10 percent deposition efficiency, such fluids will take about 9,000 years to accumulate enough ore material for a 5 Mt ore body, while poorer hydrothermal fluids (1 ppm + 1% deposition efficiency, case G in fig. 12) will never accumulate enough base metals to form a significant ore body. Results also indicate that in order to produce a supergiant ore deposit, defined here as >12 Mt of total metal, hydrothermal fluids need more than 10 ppm of base metals in solution under reasonable deposition conditions (x < 100% deposition efficiency, case D) to produce such a deposit within about 10,000 years. Alternatively, if the hydrothermal system is long-lived, a 10 ppm base metal fluid with a 10 percent deposition efficiency will take about 30,000 years to accumulate enough base metal (case E in fig. 12).

These calculations trace the thermal history of an individual fault and reflect the time-integrated accumulation of base metals as a function of temperature, fluid density, and base metal solubility. Results are based on uninterrupted fluid discharge and do not take into account tectonic events and other processes such as permeability decrease due to cooling or mineral precipitation, which might alter fluid discharge processes. While the magnitude of predicted ore bodies varies as a consequence of this as well as the type of fluid involved, most calculations suggest that less that 6,000 years of constant fluid discharge is required to form a significant ore body.

Ore body size.—Under ideal conditions (base metal saturation, 100% deposition efficiency) an ore body of phenomenal size (~10^{10} t total metal) could form; realistic estimates assuming a 10 ppm metal-carrying fluid with a 10 percent deposition efficiency yield an ore body on the order of ~35 million tonnes of total metal. By contrast, the largest VHMS deposit, Kidd Creek, contains about 12.6 million tonnes of total metal. To evaluate these predictions, a comparison with the relative size of major sulfide deposits on the modern seafloor is shown in figure 13, which compares VHMS deposits based on ore body tonnage; simulation results have been calculated assuming a 10 percent base metal content to allow comparison. Modern seafloor deposits are at the lower end of the size spectrum of massive sulfide deposits. Most are estimated to have an average size of ~0.2 Mt ore material. The TAG hydrothermal mound has been investigated more thoroughly and is estimated to be ~4 Mt (Hannington and others, 1995; Petersen and others, 2000). Calculations from this study suggest that under present modeling conditions, significantly larger ore bodies are predicted to form; ~350 Mt for fluids carrying 10 ppm base metals and a 10 percent deposition efficiency. Although there are some known massive sulfide deposits that exhibit comparable tonnage such as the Kidd Creek deposit most known ancient massive sulfide deposits are an order of magnitude smaller.

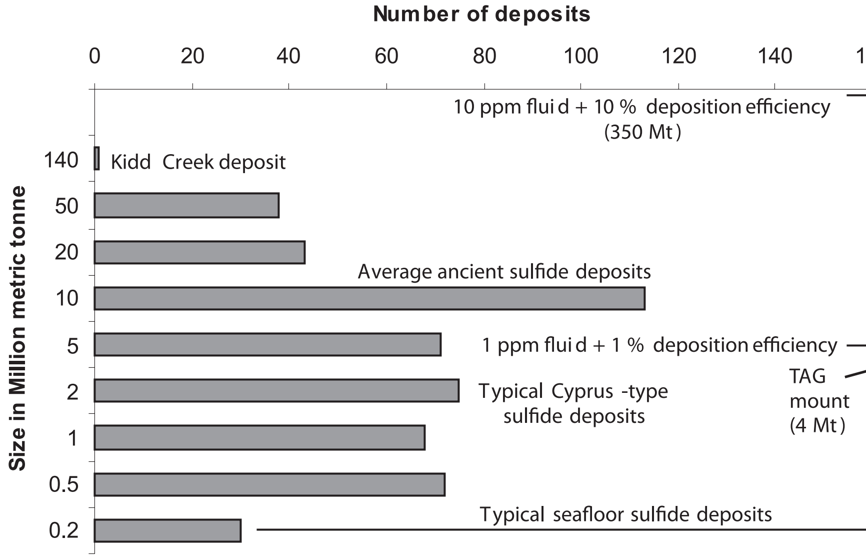

Fig. 13. Comparison of massive sulfide deposit size and ore body tonnage predicted from numerical modeling. Predicted ore bodies are significantly larger than typical modern seafloor deposits, which probably lack conditions assumed in numerical simulations (modified after Hannington and others, 1995).

Several factors may explain this discrepancy. Simulation results presented here assume that hydrothermal fluid discharge continues until the heat supply is exhausted. This is clearly not the case, as is evident from modern-day seafloor observations (Fornari and Embley, 1995; Wright, 1998). Tectonic movement, volcanic activity, and alteration are likely to interrupt established fluid flow pathways, preventing high-temperature fluid discharge at the ore site for the time spans predicted by the simulation results. Also, hydrothermal fluids are assumed to be saturated with respect to copper, lead, and zinc. Although analysis of hydrothermal fluids from present-day seafloor systems suggest that some fluids may be saturated, or even supersaturated with respect to certain base metals (Von Damm, 1995; table 5), reported metal concentrations reflect fluids that have already mixed with cold, oxidizing seawater, thereby overestimating the true metal concentrations in hydrothermal fluids as they circulate at depth and ascend to the seafloor. It is therefore reasonable to assume that *in-situ* fluids are probably not saturated with respect to base metals before mixing with other fluids and discharging onto the seafloor.

On the other hand, a hydrothermal fluid that carries no more than 10 ppm Zn + Cu in solution at any time and precipitates with low efficiency (10 percent) should form a 5 million ton ore body with a 10 percent metal content in less than 6,000 years. These calculations are based on numerical simulation results, which do not take into account additional fluid discharge for individual faults that may occur due to open side boundaries, dike intrusion, differences in fault extension or varying geometry of the numerical model. The fact that most seafloor deposits known today are probably much smaller than their ancient counterparts means that either:

a) most modern systems are unable to sustain continuous high-temperature fluid discharge for about 6,000 years for individual discharge sites. Although hydrothermal systems may last more than 100,000 years, discharge sites probably change on a frequency of less than 6,000 years,
b) the fluid chemistry is changing over this time interval to such a degree that an insufficient amount of base metals is carried in solution,

Table 5

Comparison of measured base metal concentrations in modern seafloor hydrothermal fluids with calculated saturation values

Location	Temperature (°C)	Measured concentrations Cu (ppm)	Zn (ppm)	Pb (ppm)	Calculated saturation Cu (ppm)	Zn (ppm)	Pb (ppm)
TAG[a]	301-366	9.5	25	-	0.6-8.5	63-679	-
Mid-Atlantic Ridge (Rainbow vent)[b]	360	10.3	11.7	-	7	565	-
JdFR-Endeavour[c]	350	0.9	2.2	0.007	5	411	666
Lau Basin[d]	334	2.2	197	0.4	2.7	237	512
JdFR-North[e]	262	0.4	36.8	0.07	0.08	8.7	105
JdFR-South[f]	246	0.09	49.5	0.1	0.02	3.2	65

Calculated metal solubilities are based on data by Franklin and others (1981), Ohmoto and others (1983), and Huston and Large (1987).
[a] Butterfield and Massoth (1994).
[b] Edmonds and others (1996).
[c] Charlou and others (1990), Fouquet and others (1991).
[d] Von Damm and Bishop (1987).
[e] Douville and others (2002).
[f] Butterfield and others (1994).

c) focussing mechanisms that are sufficiently efficient to channel appropriate volumes of fluids to a confined discharge site are uncommon due to certain physical changes such as permeability reduction, or
d) some other process, such as the geotectonic setting, or a combination of a, b, and c above, may prevent the widespread formation of significant massive sulfide ore deposits on the modern seafloor.

It is likely that a combination of processes prevents the formation of larger ore deposits on the seafloor, and simulation results indicate that only under certain conditions, do significant (>5 Mt) massive sulfide ore deposits form. These conditions probably include a relatively stable tectonic regime and access to an effective plumbing system tapping a sustainable heat source and effectively focussing ascending hydrothermal fluids. Of less importance seems to be the absolute metal content of the fluid or the relative precipitation efficiency. Most VHMS deposits formed in tectonically active settings, such as seafloor-dominated environments, seem to be restricted in size by the short life span of effective hydrothermal fluid discharge at any ore site, as well as their preservation potential. It is suggested that only under ideal conditions, such as a very stable geotectonic environment with good preservation potential, such as continental back-arc rift settings, will supergiant deposits form.

Ore body location and distribution.—The location of VHMS deposits relative to the associated heat source, rift axis, and stratigraphy is controlled by a) the geotectonic environment, b) the spacing and distance of fault structures relative to the heat source, and c) the permeability distribution in the subsurface. On a local scale the location of ore deposits is determined by fault spacing and the subsequent development of convection cells (as an example, recharge and discharge faults) while the location of ore bodies regionally seems to be controlled by the position of faults relative to the heat source, that is faults at topographic highs. Significant ore bodies are predicted to form above a single magma chamber and also at off-axis elevated topographic positions. Under these conditions, the occurrence of VHMS deposits is mostly a function of fault location relative to basement topography rather than fault spacing itself. Likewise, different basement/heater structures assumed to exist beneath continental rift settings might produce other ore body distribution patterns. Overall, the distribution of ore bodies will likely depend on a complex interplay between the factors discussed and, there may not necessarily exist any clearly defined or predictable distribution patterns.

CONCLUSIONS

This study describes the development and application of a numerical model to simulate heat and fluid transport in a modern back-arc type seafloor hydrothermal system to gain further insight into the evolution and development of modern seafloor hydrothermal systems with respect to hydrothermal fluid flow migration, fluid flow pathways, and other processes such as life span. While several results confirm theoretical and field observations (role of permeability, fluid discharge temperatures) numerical simulations also shed new light on critical aspects of hydrothermal systems (relationships between faults, discharge times, recharge-discharge relationships). Despite the inherent simplifications and limitations, the application of numerical modeling techniques to research the general behavior of a seafloor hydrothermal system on a regional scale has proven to be successful. New insight has been gained into how hydrothermal fluids move in the oceans crust (sheeted dikes), the localities and magnitude of hydrothermal fluid discharge (topographic heights/magma chamber) and the timing and potential of massive sulfide ore body formation (6,000 to 30,000 years). Results clearly demonstrate that rock properties (fault and rock permeability), the nature and location of fault structures, and the involved heat source are the most crucial parameters in determining the mineralogy and size of VHMS deposits while other factors may be important on a local scale. Significant ore bodies (5 Mt at 10% base metals) are predicted to form within a few thousand years of constant fluid discharge at the ore site while supergiant ore deposits (>12 Mt ore) are likely to develop in stable geotectonic terrains which can support a long-lasting hydrothermal system such as continental rift settings.

ACKNOWLEDGMENTS

This study benefited greatly from discussions with Bruce Gemmell, Mike Solomon, and Grant Garven. The senior author would also like to acknowledge the financial support of the Australian Research Council and the Centre for Ore Deposit Research at the University of Tasmania. The authors also thank the reviewers for their constructive and helpful comments.

REFERENCES

Alt, J. C., 1995, Subseafloor processes in mid-ocean ridge hydrothermal systems: Geophysical Monograph no. 91, p. 85–114.

Alt, J. C., Laverne, C., and Muehlenbachs, K., 1985, Alteration of the upper oceanic crust: Mineralogy and processes in Deep Sea Drilling Project hole 504B, Leg 83: Initial Reports of the Deep Sea Drilling Project, v. 83, p. 217–241.

Alt, J. C., Honorrez, J., Laverne, C., and Emmermann, R., 1986, Hydrothermal alteration of a 1 km section through the upper oceanic crust, Deep Sea Drilling Project hole 504B: Mineralogy, chemistry, and evolution of seawater–basalt interactions: Journal of Geophysical Research, v. 91, p. 10,309–10,335.

Alt, J. C., Teagle, D. A. H., Brewer, T., Shanks W. C., III, and Halliday, A., 1998, Alteration and mineralization of an oceanic forearc and the ophiolite-ocean crust analogy: Journal of Geophysical Research, v. 103, p. 12,365–12,380.

Barrie, C. T., Cathles, L. M., and Erendi, A., 1999a, Finite element heat and fluid-flow computer simulations of a deep ultramafic sill model for the Giant Kidd Creek volcanic-associated massive sulfide deposit, Abititi Subprovince, Canada: Economic Geology Monograph no. 10, p. 529–540.

Barrie, C. T., Cathles, L. M., Erendi, A., Schwaiger, H., and Murray, C., 1999b, Heat and fluid-flow in volcanic-associated massive sulfide-forming hydrothermal systems: Reviews in Economic Geology, v. 8, p. 201–219.

Bear, J., 1972, Dynamics of fluids in porous media: New York, American Elsevier, 764 p.

Becker, K., 1990, Measurement of the permeability of the upper oceanic crust at hole 395A, ODP Leg 109: Proceedings of the Ocean Drilling Program, Scientific Results, v. 106/109, p. 213–222.

Becker, K., Langseth, M. G., and Von Herzen, R. P., 1985, Deep crustal geothermal measurements, Hole 504B, Deep Sea Drilling Project legs 69, 70, 83, and 92: Deep Sea Drilling Project, v. 83, p. 405–418.
Becker, K., Sakai, H., Merrill, R. B., Adamson, A. C., Alexandrovich, J., Alt, J. C., Anderson, R. N., Bideau, D., Gable, R., Herzig, P. M., Houghton, S., Ishizuka, H., Kawahata, H., Kinoshita, H., Lovell, M. A., Malpas, J., Masuda, H., Morin, R. H., Mottl, M. J., Pariso, J. E., Pezard, P., Phillips, J., Sparks, J., and Uhlig, S., 1989, Measurements of the permeability of the sheeted dikes in Hole 504B, ODP Leg 111: Proceedings of the Ocean Drilling Program, Scientific Results, v. 111, p. 317–325.
Brauhart, C. W., Groves, D., and Morant, P., 1998, Regional alteration systems associated with volcanogenic massive sulfide mineralization at Panorama, Pilbara, Western Australia: Economic Geology, v. 93, p. 292–303.
Bruns, T. R., and Lavoie, D. L., 1994, Bulk permeability of young back arc basalt in the Lau basin from a downhole packer experiment: Proceedings of the Ocean Drilling Program, Scientific Results, v. 135, p. 805–816.
Butterfield, D. A., and Massoth, G. J., 1994, Geochemistry of North Cleft segment vent fluids: temporal changes in chlorinity and their possible relation to recent volcanism: Journal of Geophysical Research, v. 99, p. 4,951–4,968.
Butterfield, D. A., McDuff, R. E., Mottl, M. J., Lilley, M. D., Lupton, J. E., and Massoth, G. J., 1994, Gradient in the composition of hydrothermal fluids from the Endeavour Ridge vent field: Phase separation and brine loss: Journal of Geophysical Research, v. 99, p. 9,561–9,583.
Cann, J. R., Strens, M. R., and Rice, A., 1985/86, A simple magma–driven thermal balance model for the formation of volcanogenic massive sulphides: Earth and Planetary Science Letters, v. 76, p. 123–134.
Cathles, L. M., 1983, An analysis of the hydrothermal system responsible for massive sulfide deposition in the Hokuroku Basin of Japan: Economic Geology Monograph no. 5, p. 439–487.
——— 1993, A capless 350 degrees C flow zone model to explain megaplumes, salinity variations, and high-temperature veins in ridge axis hydrothermal systems: Economic Geology, v. 88, p. 1,975–1,986.
Cathles, L. M., Erendi, A. H. J., and Barrie, T., 1997, How long can a hydrothermal system be sustained by a single intrusive event?: Economic Geology, v. 92, p. 766–771.
Charlou, J. L., Donval, J. P., Caprais, M. P., Erzinger, J., Fouquet, Y., and Von Stackelberg, U., 1990, Hydrothermal activity in the Lau back arc basin; plumes and hot fluids chemistry: American Association of Petroleum Geologists Bulletin, v. 74, p. 963–964.
Christiansen, L. B., and Iturrino, G. J., 2004, Core-scale permeability of an actively venting, felsic-hosted hydrothermal system: the PACMANUS hydrothermal field: Proceedings of the Ocean Drilling Program, Scientific Results, v. 192, p. 1–19.
Collier, J. S., and Sinha, M. C., 1992, Seismic mapping of a magma chamber beneath the Valu Fa ridge, Lau Basin: Journal of Geophysical Research, v. 97, p. 14,031–14,053.
Converse, D. R., Holland, H. D., and Edmond, J. M., 1984, Flow rates in the axial hot springs of the East Pacific Rise (21°N): implications for the heat budget and the formation of massive sulfide deposits: Earth and Planetary Science Letters, v. 69, p. 159–175.
Curewitz, D., and Karson, J. A., 1997, Structural settings of hydrothermal outflow: fracture permeability maintained by fault propagation and interaction: Journal of Volcanology and Geothermal Research, v. 79, p. 149–168.
Davis, E. E., Chapman, D. S., Forster, C. B., and Villinger, H., 1989, Heat-flow variations correlated with buried basement topography on the Juan de Fuca Ridge flank: Nature, v. 342, p. 533–537.
Davis, E. E., Chapman, D. S., and Forster, C. B., 1996, Observations concerning the vigour of hydrothermal circulation in young oceanic crust: Journal of Geophysical Research, v. 101, p. 2,927–2,942.
Dickson, P., Schulz, A., and Woods, A., 1995, Preliminary modeling of hydrothermal circulation within mid-ocean ridge sulphide structures: Geological Society of London Special Publication, v. 87, p. 145–157.
Douville, E., Charlou, J. L., Oelkers, E. H., Bienvenu, P., Jove Colon, C. F., Donval, J. P., Fouquet, Y., Prieur, D., and Appriou, P., 2002, The Rainbow Vent fluids (36 degrees 14′N, MAR): the influence of ultramafic rocks and phase separation on trace metal content in Mid–Atlantic Ridge hydrothermal fluids: Chemical Geology, v. 184, p. 37–48.
Edmonds, H. N., German, C. R., Green, D. R. H., Huh, Y., Gamo, T., and Edmond, J. M., 1996, Continuation of the hydrothermal fluid chemistry time series at TAG, and the effects of ODP drilling: Geophysical Research Letters, v. 23, p. 3,487–3,489.
Elderfield, H., Becker, K., and Davis, E. E., 2004, Foundations of research into heat, fluid, and chemical fluxes in oceanic crust, *in* Davis, E. E., and Elderfield, H., editors, Hydrogeology of the oceanic lithosphere: Cambridge, Cambridge University Press, p. 28–56.
Fehn, U., and Cathles, L., 1979, Hydrothermal convection at slow-spreading mid-ocean ridges: Tectonophysics, v. 55, p. 239–260.
Fisher, A. T., 1998, Permeability within basaltic oceanic crust: Reviews of Geophysics, v. 36, p. 143–182.
——— 2004, rates of flow and patterns of fluid circulation, *in* Davis, E. E., and Elderfield, H., editors, Hydrogeology of the oceanic lithosphere: Cambridge, Cambridge University Press, p. 337–375.
Fisher, A. T., and Becker, K., 1995, Correlation between seafloor heat flow and basement relief; observational and numerical examples and implications for upper crustal permeability: Journal of Geophysical Research, v. 100, p. 12,641–12,657.
Fisher, A. T., and Narasimhan, T. N., 1991, Numerical simulations of hydrothermal circulation resulting from basalt intrusions in a buried spreading center: Earth and Planetary Science Letters, v. 103, p. 100–115.
Fisher, A. T., Becker, K., Narasimhan, T. N., Langseth, M. G., and Mottl, M. J., 1990, Passive, off-axis

convection through the southern flank of the Costa Rica Rift: Journal of Geophysical Research, v. 95, p. 9,343–9,370.
Fisher, A. T., Becker, K., and Narasimhan, T. N., 1994, Off-axis hydrothermal circulation: parametric tests of a refined model of processes at Deep Sea Drilling Project/Ocean Drilling Program site 504: Journal of Geophysical Research, v. 99, p. 3,097–3,121.
Fisher, A. T., Becker, K., and Davis, E. E., 1997, The permeability of young oceanic crust east of Juan de Fuca Ridge determined using borehole thermal measurements: Geophysical Research Letters, v. 24, p. 1,311–1,314.
Fontaine, F. J., Rabinowicz, M., and Boulègue, J., 2001, Permeability changes due to mineral diagenesis in fractured crust: implications for hydrothermal circulation at mid-ocean ridges: Earth and Planetary Science Letters, v. 184, p. 407–425.
Fornari, D., and Embley, R. W., 1995, Tectonic and volcanic controls on hydrothermal processes at the mid-ocean ridge: An overview based on near-bottom and submersible studies: Geophysical Monograph no. 91, p. 1–46.
Fouquet, Y., von Stackelberg, U., Chalou, J. L., Donval, J. P., Erzinger, J., Foucher, J. P., Herzig, P. M., Mühe, R., Soakai, S., Wiedicke, M., and Whitechurch, H., 1991, Hydrothermal activity in the Lau back-arc basin: Sulfides and water chemistry: Geology, v. 19, p. 303–306.
Fouquet, Y., von Stackelberg, U., Chalou, J. L., Erzinger, J., Herzig, P. M., Mühe, R., and Wiedecke, M., 1993, Metallogenesis in back-arc environments: The Lau Basin example: Economic Geology, v. 88, p. 2,154–2,181.
Franklin, J. M., Lydon, J. W., and Sangster, D. F., 1981, Volcanic-associated massive sulfide deposits: Economic Geology 75th Anniversary Volume, p. 485–627.
Frenzel, G., Mühe, R., and Stoffers, P., 1990, Petrology of the volcanic rocks of the Lau Basin, southwest Pacific: Geologisches Jahrbuch, v. 92, p. 395–479.
Galley, A. G., 1993, Characteristics of semi-conformable alteration zones associated with volcanogenic massive sulphide districts: Journal of Geochemical Exploration, v. 48, p. 175–199.
Giambalvo, E. R., Fisher, A. T., Martin, J. T., Darty, L., and Lowell, R. P., 2000, Origin of elevated sediment permeability in a hydrothermal seepage zone, eastern flank of the Juan de Fuca Ridge, and implications for transport of fluids and heat: Journal of Geophysical Research, v. 105, p. 913–928.
Gill, J. B., 1976, Composition and age of the Lau Basin and Ridge volcanic rocks: Implications for evolution of an interarc basin and remnant arc: Geological Society of America Bulletin, v. 87, p. 1,384–1,395.
Gillis, K. M., and Robinson, P. T., 1988, Distribution of alteration zones in the upper oceanic crust: Geology, v. 16, p. 262–266.
Ginster, U., Mottl, M. J., and Von Herzen, R. P., 1994, Heat flux from black smokers on the Endeavour and Cleft segments, Juan de Fuca Ridge: Journal of Geophysical Research, v. 99, p. 4,937–4,950.
Goldberg, D., Broglia, C., and Becker, K., 1991, Fracturing, alteration, and permeability: In–situ properties in hole 735B: Proceedings of the Ocean Drilling Program, Scientific Results, v. 118, p. 261–269.
Green, K. E., Von Herzen, R. P., and Williams, D. L., 1981, The Galapagos spreading center at 86 degrees W; a detailed geothermal field study: Journal of Geophysical Research, v. 86, p. 979–986.
Hannington, M. D., Jonasson, I. R., Herzig, P. M., and Petersen, S., 1995, Physical and chemical processes of seafloor mineralization at mid-ocean ridges: Geophysical Monograph no. 91, p. 115–157.
Hawkins, J. W., 1995, Evolution of the Lau Basin-Insight from ODP Leg 135: Geophysical Monograph, v. 88, p. 125–173.
Herzig, P. M., Von Stackelberg, U., and Petersen, S., 1990, Hydrothermal mineralization from the Valu Fa Ridge, Lau back-arc basin (SW Pacific): Marine Mining, v. 9, p. 271–301.
Herzig, P. M., Hannington, M. D., Fouquet, Y., Von Stackelberg, U., and Petersen, S., 1993, Gold-rich polymetallic sulfides from the Lau back arc and implications for the geochemistry of gold in sea-floor hydrothermal systems of the Southwest Pacific: Economic Geology, v. 88, p. 2,182–2,209.
Herzig, P. M., Hannington, M. D., and Arribas, A., Jr., 1998, Sulfur isotopic composition of hydrothermal precipitates from the Lau back-arc: implications for magmatic contributions to seafloor hydrothermal systems: Mineralium Deposita, v. 33, p. 226–237.
Hodkinson, R. A., and Cronan, D. S., 1998, Hydrothermal inputs at ODP Sites 836, 838 and 839 in relation to Eastern Lau Spreading Centre propagation in the Lau basin, southwest Pacific, *in* Cramp, A., MacLeod, C. J., Lee, S. V., and Jones, E. W., editors, Geological evolution of ocean basins: Results from the Ocean Drilling Program: Geological Society of London, Special Publication, v. 131, p. 231–242.
Huston, D. L., and Large, R. R., 1987, Genetic and exploration significance of the zinc ratio (100 Zn/(Zn + Pb)) in massive sulfide systems: Economic Geology, v. 82, p. 1,521–1,539.
Huyakorn, P. S., and Pinder, G. F., 1983, Computational methods in subsurface flow: New York, Academic Press, 473 p.
Ingebritsen, S. E., and Sanford, W. E., 1998, Groundwater in geological processes: New York, Cambridge University Press, 341 p.
Kamenetsky, V., Crawford, T., Eggins, S., and Muehe, R., 1997, Phenocryst and melt inclusion chemistry of near-axis seamounts, Valu Fa Ridge, Lau Basin; insight into mantle wedge melting and the addition of subduction components: Earth and Planetary Science Letters, v. 151, p. 205–223.
Kent, A. J. R., Peate, D. W., Newman, S., Stopler, E. M., and Pearce, J. A., 2002, Chlorine in submarine glasses from the Lau Basin: seawater contamination and constraints on the composition of slab-derived fluids: Earth and Planetary Science Letters, v. 202, p. 361–377.
Lagabrielle, Y., Auzende, J. M., Eissen, J. P., Janin, M. C., and Cotton, J., 1994, Geology and geochemistry of a 800 m section through young upper oceanic crust in the North Fiji Basin (Southwest Pacific): Marine Geology, v. 116, p. 113–132.
Large, R. R., 1992, Australian volcanic-hosted massive sulfide deposits: features, styles, and genetic models: Economic Geology, v. 87, p. 471–510.

Large, R. R., and Blundell, D., 2000, GEODE Database in global VMS districts: University of Tasmania CODES Publication, 179 p.

Lentz, D. R., 1998, Petrogenetic evolution of felsic volcanic sequences associated with Phanerozoic volcanic-hosted massive sulphide systems: the role of extensional geodynamics: Ore Geology Review, v. 12, p. 289–327.

Lister, C. R. B., 1972, On the thermal balance of a mid-ocean ridge: Geophysical Journal International, v. 26, p. 515–535.

Lowell, R. P., 1980, Topographically driven subcritical hydrothermal convection in the oceanic crust: Earth and Planetary Science Letters, v. 49, p. 21–28.

——— 1991, Modeling continental and submarine hydrothermal systems: Review in Geophysics, v. 29, p. 457–476.

Lowell, R. P., and Burnell, D. K., 1991, Mathematical modeling of conductive heat transfer from a freezing, convecting magma chamber to a single-pass hydrothermal system: implications for seafloor black smokers: Earth and Planetary Science Letters, v. 104, p. 59–69.

Lowell, R. P., and Germanovich, L. N., 1994, On the thermal evolution of high-temperature hydrothermal systems at ocean ridge crests: Journal of Geophysical Research, v. 99, p. 565–575.

Lowell, R. P., and Yao, Y., 2002, Anhydrite precipitation and the extent of hydrothermal recharge zones at ocean ridge crests: Journal of Geophysical Research, v. 107, p. EPM 2-1–2-9.

Lowell, R. P., Rona, P. A., and Von Herzen, R. P., 1995, Seafloor hydrothermal systems: Journal of Geophysical Research, v. 100, p. 327–352.

Lowell, R. P., Yao, Y., and Germanovich, L. N., 2003, Anhydrite precipitation and the relationship between focused and diffuse flow in seafloor hydrothermal systems: Journal of Geophysical Research, v. 108, doi:10.1029/2002JB002371.

Lydon, J. W., 1988, Ore deposit models #14, volcanogenic massive sulphide deposits Part 2: Genetic models: Geoscience Canada, v. 15, p. 43–65.

——— 1996, Characteristics of volcanogenic massive sulphide deposits: Interpretation in terms of hydrothermal convection systems and magmatic hydrothermal systems: Instituto Geominero de Espana, Boletin geológico y minero, v. 107, p. 215–264.

MacPherson, C. G., and Mattey, D. P., 1998, Oxygen isotope variations in Lau basin: Chemical Geology, v. 144, p. 177–194.

Martin, J. T., and Lowell, R. P., 1997, On thermoelasticity and silica precipitation in hydrothermal systems: Numerical modeling of laboratory experiments: Journal of Geophysical Research, v. 102, p. 12,095–12,107.

McCollom, T. M., and Shock, E. L., 1998, Fluid-rock interaction in the lower oceanic crust: thermodynamic models of hydrothermal alteration: Journal of Geophysical Research, v. 103, p. 547–575.

Morton, J. L., and Sleep, N. H., 1985, Seismic reflections from a Lau Basin magma chamber, *in* Scholl, D. W., and Vallier, T. L., editors, Geology and offshore resources of Pacific island arcs-Tonga region: Circum-pacific Council for Energy and Mineral Resources Earth Science Series, v. 2, p. 441–453.

Mottl, M. J., 1983, Metabasalts, axial hot springs, and the structure of hydrothermal systems at mid-ocean ridges: Geological Society of America Bulletin, v. 94, p. 161–180.

Ohmoto, H., Mizukami, M., Drummond, S. E., Eldridge, C. S., Pisutha-Arnond, V., and Lenagh, T. C., 1983, Chemical processes of Kuroko formation: Economic Geology Monograph no. 5, p. 570–604.

Parmentier, E. M., and Spooner, E. T. C., 1978, A theoretical study of hydrothermal convection and the origin of the ophiolitic sulphide ore deposits of Cyprus: Earth and Planetary Science Letters, v. 40, p. 33–44.

Parson, L. M., and Wright, I. C., 1996, The Lau-Havre-Taupo back-arc basin: a southward-propagating, multi-stage evolution from rifting to spreading: Tectonophysics, v. 263, p. 1–22.

Parson, L. M., Rothwell, R. G., and MacLeod, C. J., 1994, Tectonics and sedimentation in the Lau Basin (Southwest Pacific): Proceedings of the Ocean Drilling Program, Scientific Results, v. 135, p. 9–21.

Petersen, S., Herzig, P. M., and Hannington, M. D., 2000, Third dimension of a presently forming VMS deposit; TAG hydrothermal mound, Mid-Atlantic Ridge, 26N.: Mineralium Deposita, v. 35, p. 233–259.

Rabinowicz, M., Boulegue, J., and Genthon, P., 1998, Two- and three-dimensional modeling of hydrothermal convection in the sedimented Middle Valley segment, Juan de Fuca Ridge: Journal of Geophysical Research, v. 103, p. 24,045–24,065

Raffensperger, J. P., and Garven, G., 1995, Fluid flow and geochemical modeling in sediment-hosted ore systems: St. Louis, Missouri, International Field Conference on Carbonate-hosted Lead-zinc Deposits, workshop manual, 125 p.

Richardson, C. J., Cann, J. R., Richards H. G., and Cowan, J. G., 1987, Metal-depleted root zones of the Troodos ore-forming hydrothermal systems, Cyprus: Earth and Planetary Science Letters, v. 84, p. 243–253.

Riech, V., Marchig, V., Sunkel, G., and Weiss, W., 1990, Hydrothermal and volcanic input in sediments of the Lau back-arc Basin, SW Pacific: Marine Mining, v. 9, p. 183–203.

Rosenberg, N. D., and Spera, F. J., 1992, Convection in porous media with thermal and chemical buoyancy; a comparison of two models for solute dispersion: The IMA Volumes in Mathematics and its Applications, v. 41, p. 225–235.

Rosenberg, N. D., Spera, F. J., and Haymon, R. M., 1993, The relationship between flow and permeability field in seafloor hydrothermal systems: Earth and Planetary Science Letters, v. 116, p. 135–153.

Rothwell, R. G., 1998, Sedimentary evidence relating to the tectonic evolution of the Lau Basin, SW Pacific, from ODP Sites 834–839 (ODP Leg 135), *in* Cramp, A., MacLeod, C. J., Lee, S. V., and Jones, E. J. W., editors, Geological evolution of ocean basins: Results from the Ocean Drilling Program: Geological Society of London, Special Publication, v. 131, p. 211–229.

Salisbury, M. H., Christensen, N. I., and Becker, K., 1985, The velocity structure of layer 2 at deep sea drilling

project site 504 from logging and laboratory experiments: Initial Reports of the Deep Sea Drilling Project, v. 83, p. 529–539.
Schardt, C., ms, 2004, Heat and fluid flow simulations in submarine volcanic terrains and implications for the formation of massive sulfide deposits: Tasmania, University of Tasmania, Ph.D. thesis, 304 p.
Schardt, C., Yang, J., and Large, R. R., 2005, Numerical heat and fluid flow modeling of the Panorama volcanic-hosted massive sulfide district, Western Australia: Economic Geology, v. 100, p. 547–566.
Singer, D. A., 1995, World-class base and precious metal deposits; a quantitative analysis: Economic Geology, v. 90, p. 88–104.
Sinton, J. M., and Detrick, R. S., 1992, Mid-ocean ridge magma chambers: Journal of Geophysical Research, v. 97, p. 197–216.
Sleep, N. H., 1991, Hydrothermal circulation, anhydrite precipitation, and thermal structure at ridge axes: Journal of Geophysical Research, v. 96, p. 2,375–2,387.
Snelgrove, S. H., and Forster, C. B., 1996, Impact of seafloor sediment permeability and thickness on off-axis hydrothermal circulation: Juan de Fuca Ridge eastern flank: Journal of Geophysical Research, v. 101, p. 2,915–2,925.
Solomon, M., Walshe, J. L., and Eastoe, C. J., 1987, Experiments on convection and their relevance to the genesis of massive sulphide deposits: Australian Journal of Earth Sciences, v. 34, p. 311–323.
Sparks, R. S. J., 1986, The role of crustal contamination in magma evolution through time: Earth and Planetary Science Letters, v. 78, p. 211–223.
Spivack, A. J., and Edmond, J. M., 1987, Boron isotope exchange between seawater and the ocean crust: Geochimica et Cosmochimica Acta, v. 51, p. 1,033–1,043.
Stanton, R. L., 1991, Understanding volcanic massive sulfides; past, present, and future: Economic Geology Monograph no. 8, p. 82–95.
Strens, M. R., and Cann, J. R., 1982, A model of hydrothermal circulation in fault zones at mid-ocean ridge crests: Geophysical Journal of the Royal Astronomical Society, v. 71, p. 225–240.
—— 1986, A fracture–loop thermal balance model of black smoker circulation: Tectonophysics, v. 122, p. 307–324.
Sunkel, G., 1990, Petrology and geochemistry of submarine lavas from the Lau basin (SW Pacific): Marine Mining, v. 9, p. 205–234.
Tappin, D. R., Bruns, T. R., and Geist, E. L., 1994, Rifting of the Tonga/Lau ridge and formation of the Lau back arc basin: Evidence from site 840 on the Tonga ridge: Proceedings of the Ocean Drilling Program, Scientific Results, v. 135, p. 367–371.
Turner, I. M., Peirce, C., and Sinha, M. C., 1999, Seismic imaging of the axial region of the Valu Fa ridge, Lau Basin—the accretionary processes of an intermediate back-arc spreading ridge: Geophysical Journal International, v. 138, p. 495–519.
Vallier, T. L., Jenner, G. A., Frey, F. A., Gill, J. B., Davis, A. S., Volpe, A. M., Hawkins, J. W., Morris, J. D., Cawood, P. A., Morton, J. L., Scholl, D. W., Rautenschlein, M., White, W. M., Williams, R. W., Stevenson, A. J., and White, L. D., 1991, Subalkaline andesite from Valu Fa Ridge, a back-arc spreading center in southern Lau Basin: petrogenesis, comparative chemistry, and tectonic implications: Chemical Geology, v. 91, p. 227–256.
Varga, R. J., Gee, J. S., Bettison-Varga, L., Anderson, R. S., and Johnson, C. L., 1999, Early establishment of seafloor hydrothermal systems during structural extension: palaeomagnetic evidence from the Troodos ophiolite, Cyprus: Earth and Planetary Science Letters, v. 171, p. 221–235.
Von Damm, K. L., 1995, Controls on the chemistry and temporal variability of seafloor hydrothermal fluids: Geophysical Monograph no. 91, p. 222–247.
Von Damm, K. L., and Bishop, J. L., 1987, Chemistry of hydrothermal solutions from the Southern Juan de Fuca Ridge: Journal of Geophysical Research, v. 92, p. 11,334–11,346.
Von Stackelberg, U., and Von Rad, U., 1994, Back-arc hydrothermal activity in the Lau basin (Sonne cruises SO35 and SO48), *in* Stevenson, A. J., Herzer, R. H., and Balance, P. F., editors, Geology and submarine resources of the Tonga-Lau-Fiji region: SOPAC Technical Bulletin, v. 8, p. 307–318.
Wiedicke, M., and Collier, J., 1993, Morphology of the Valu Fa Spreading Ridge in the Southern Lau Basin: Journal of Geophysical Research, v. 98, p. 11,769–11,782.
Wright, D. J., 1998, Formation and development of fissures at the East Pacific rise: Implications for faulting and magmatism at mid-ocean ridges: Geophysical Monograph no. 106, p. 137–151.
Yang, J., 2002, Influence of normal faults and basement topography on ridge-flank hydrothermal fluid circulation: Geophysical Journal International, v. 151, p. 83–87.
Yang, J., and Large, R. R., 2001, Computational modeling of hydrothermal ore-forming fluid migration in complex earth structures, *in* Xie, H., Wang, Y., and Jiang, Y., editors, Computer Applications in the Minerals Industry: Lisse, A. A. Balkema, p. 115–120.
Yang, J., Latychev, K., and Edwards, R. N., 1998, Numerical computation of hydrothermal fluid circulation in fractured Earth structures: Geophysical Journal International, v. 135, p. 627–649.
Yang, J., Large, R., and Bull, S., 2001, Factors controlling fluid discharge and recharge in faults associated with free convection hydrothermal systems: American Geophysical Union, Chapman Conference, Perth, p. 11–14.